# Investigation of underwater shield tunnel excavation face stability in lower dense and upper loose strata

**Fei Jia**
Beijing University of Technology
**Chuang Wang**
Beijing University of Technology
**Pengfei Li**
lpf@bjut.edu.cn

Beijing University of Technology
**Xiaopu Cui**
Beijing University of Technology
**Qing Xu**
Beijing University of Technology
**Zhaoguo Ge**
China Railway Construction Corporation (China)

**Research Article**

**Keywords:** Lower dense and upper loose strata, Underwater shield tunnel, Stability of the excavation face, Various depths

**Posted Date:** February 9th, 2026

**DOI:** https://doi.org/10.21203/rs.3.rs-8760248/v1



**Additional Declarations:** No competing interests reported.

# Investigation of underwater shield tunnel excavation face stability in lower dense and upper loose strata

Fei Jia [a, b], Chuang Wang[a], Pengfei Li[a,*], Xiaopu Cui[a], Qing Xu[a], Zhaoguo Ge[c]

[a] *Key Laboratory of Urban Security and Disaster Engineering, Ministry of Education, Beijing University of Technology, Beijing 100124, China;*

[b] *China Railway No.3 Engineering Group No.4 Engineering Co., Ltd., Beijing 102300, China;*

[c] *China Railway 14th Corporation Mega Shield Construction Engineering Co. Ltd., Nanjing 211800, China.*

*Corresponding author. E-mail address: lpf@bjut.edu.cn

**Abstract:** In order to study the stability of the excavation face in the lower dense and upper loose, saturated sandy-pebble strata, physical model tests are conducted. The study concentrated on researching the progressing failure laws of the shield tunnel excavation face under various buried depths, and numerical simulations are employed to confirm the test results. Meanwhile, the theory calculation model of excavation face adapted to this stratum is put forward, and the theoretical formula of limited effective support compressive stress is presented. The results indicated that, as the baffle moves, the peak displacements of surface settlement successively occur in stages of no settlement, slow settlement and rapid settlement. The decrease of buried depth will increase the magnitude and range of surface settlement and will break the limiting state of equilibrium of the strata faster. Simultaneously, the decrease of buried depth will accelerate the seepage velocity of water in the strata without affecting the range of seepage path of water. In addition, the decreased burial depth will increase unstable range of the stratum. Under the equal burial depth, the unstable range of the lower dense and upper loose is bigger than that of homogeneous strata. Finally, the limit effective support compressive stress decreases with reduced burial depth.

**Keywords**: Lower dense and upper loose strata; Underwater shield tunnel; Stability of the excavation face; Various depths

## 1 Introduction

When traversing rivers, lakes, and seas, the construction of underwater shield tunnels offers distinct advantages over traditional bridge construction, including minimal disruption to water traffic, resilience against adverse weather conditions, and flexibility in terms of construction location. It is very important that the excavation face is stable when building an underwater shield tunnel. This is because it affects how safe the construction process is and how stable the tunnel will be in the long term (Zhang et al. 2022a; Di et al. 2022).

Currently, the excavation stability of tunnels is typically studied using theory analysis, numerical simulation, and model tests. Theoretical analysis methods can be applied to various geological conditions and clarify the instability mechanisms of excavation faces. The two main theoretical analysis methods are the limit equilibrium method (Ding et al. 2022; Wang et al. 2023a; Li et al. 2023; Lei et al. 2024) and the limit analysis method (Yang and Zhong 2019; Yi et al. 2019; Antão et al. 2021; Cheng et al. 2023a; Kong et al. 2024; Yang et al. 2024). The limit equilibrium method is based on the assumption that the excavation face of a tunnel is in a critical state, and proposes a potential failure mechanism. For example, Han et al. (2021) proposed a stability model of excavation face which is suitable for crossing the fault fracture zone of high hydraulic pressure, which is composed of a trapezoid and a prism. Liu et al. (2019) proposed an excavation face failure model consisting of rotational and gravitational damage zones for sand strata. The limit analysis method, based on plastic theory, solves for the limit support force of the excavation face by applying the upper-bound theorem (Ding et al. 2019; Zhang et al. 2019; Cui et al. 2025a) and lower-bound theorem (Habumuremyi and Xiang 2023). Meanwhile, the limit analysis method is a more accurate way of describing how the excavation face fails when there is seepage (Li et al. 2021; Hou and Yang 2022).

Numerical simulation method exhibits strong adaptability in addressing complex geological conditions and multi-field coupling issues. It is based on the finite element method (Alagha and Chapman 2019; Ma et al. 2022b; Ge et al. 2024; Chen et al. 2024), finite difference method (Ye et al. 2022; Cheng et al. 2023b; Cui et al. 2024) and discrete element method (Wang et al. 2022; Fu et al. 2022) to simulate and analyze the excavation face of shield tunnel in two-dimensional or three-dimensional. Among them, the finite element method can be coupled with the physical field such as seepage field,

which is suitable for the analysis of the stability of the excavation face in saturated strata (Lu et al. 2017; Wang et al. 2019). The discrete element method can deal with the motion process of discrete particles well, and is suitable for simulating local failure and collapse in the process of excavation face instability. For sand-gravel inclined strata, Tu et al. (2024) investigated the effect of the inclined angle of the strata on the limit support force of the excavation face. Wang et al. (2024) obtained the law that with the increase of cutterhead opening rate and rotating speed, the local failure area in cobble-rich soil gradually increases.

The model test method can visually show the progressive instability process of strata, which is convenient for observing the failure mechanism of the excavation face. Gravity model test (Hu et al. 2021; Di et al. 2024) and centrifugal model test (Wong et al. 2012; Yin et al. 2021) are commonly used in physical model test. Due to the low cost of gravity model tests and ease of repetition, scholars have done plenty of studies about the stability of excavation faces for sand strata (Lü et al. 2018; Zhao et al. 2024) and clay strata (Ma et al. 2022a; Jia et al. 2023). The centrifugal model test's stress field aligns with standard practice, offering a more authentic reflection of strata failure processes. Through a series of centrifugal model tests, Chen et al. (2018) obtained the impact of different water pressure on the limit support force of excavation face in sand strata. Weng et al. (2020) obtained the progressive failure mechanism of excavation face under different longitudinal slope angles for clay strata. Cui et al. (2025b) studied the failure mechanism of excavation surfaces in inclined water-rich strata with different inclination angles. Cui et al. (2025c) also investigated the failure mechanism of excavation surfaces in water-rich, silty clay overlying sandy cobble strata under differing seepage conditions.

Sandy pebble strata is widely distributed in Beijing, Chengdu and other cities in China. The sandy pebble strata are characterized by uneven particle size, large porosity and good water permeability. Due to the strong dispersibility of sandy pebble strata, it is significantly different from the engineering properties of sand strata and clay strata (Wang et al. 2023b). If the shield tunnel is constructed in saturated sandy pebble strata, phenomena such as leakage of water and ground collapse are likely to occur. Due to the strata deposition, the actual sandy pebble strata are usually loose in the upper part and dense in the lower part, but the current researches only focus on the homogeneous sandy pebble strata (Lin et al. 2021; Di et al. 2023). Meanwhile, the burial depth will have a

important effect on the failure mechanism for excavation face (Zhang et al. 2022b; Liu et al. 2024).

This study focuses on a section of Chengdu Metro Line 17 as the engineering background, utilizing model tests to investigate the lower dense and upper loose saturated sandy pebble strata. Numerical simulations are developed to compare and verify the results of model tests. By combining model tests and numerical simulations, this research aims to explore the progressive failure laws of shield tunnel excavation face with active instability for various buried depths. Meanwhile, a theoretical calculation model suitable for this formation is proposed, and the analytical formula of the limit effective support pressure on excavation face under the seepage condition is derived. This is of great significance to ensure the construction safety of similar projects.

## 2 Project Background

The dual-track tunnel of Chengdu Metro Line 17 Jiujiang North station to Baifo Bridge station passes under the Jiang 'an River, and the metro tunnel is constructed by shield method. The tunnel is 7.5 meters wide, and the distance from the top of the tunnel to the bottom of the river is about 15 meters. The strata through which the tunnel passes are mainly slightly, medium and dense sandy pebble strata. The tunnel is primarily driven at the junction of the medium-dense and dense sandy pebble strata. The left line tunnel is selected, and the geographical location of the shield section and stratigraphic profile are shown in Fig. 1, and Table 1 shows the physical and mechanical parameters of the stratum.

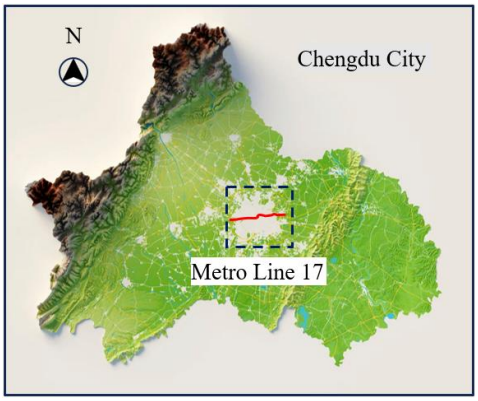


(a) Metro line 17


(b) Jiujiang North station-Baifo Bridge station


(c) Geographic location of the Jiang'an River

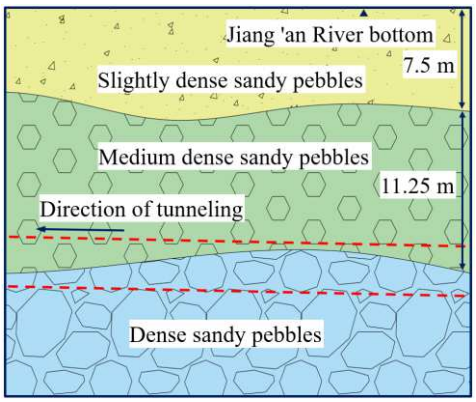


(d) Stratigraphic profile

**Fig. 1.** Geographical location of the shield section and stratigraphic profile.

**Table 1.** Physical and mechanical parameters of the strata.

| Classification of strata | Saturated unit weight $\gamma$ (kg/m$^3$) | Internal friction angle $\varphi$ (°) | Young's modulus $E$ (MPa) | Poisson's ratio $\mu$ | Relative compactness $D_r$ |
|---|---|---|---|---|---|
| Slightly dense sandy pebble | 1900 | 38 | 18 | 0.27 | 0.33 |
| Medium dense sandy pebble | 2100 | 42 | 38 | 0.24 | 0.57 |
| Dense sandy pebble | 2300 | 45 | 50 | 0.22 | 0.78 |

## 3 Test design

### 3.1 Test device and scheme

The stability of the excavation face is studied using an indoor model test device (Mi and Xiang 2020), as illustrated in Fig. 2. The model box side wall is made of a transparent acrylic plate, and a semi-cylindrical shield tunnel with an inner diameter of 30 cm has been set up on it. The excavation face control system is composed of a fixed plastic plate with holes and a movable baffle, and the plastic plate with holes is used to simulate the cutterhead during shield excavation. The baffle is made of wire mesh and sponge. This allows water to pass through while preventing soil from doing so. The water is returned to the strata surface by a water pump through the baffle, so that the water level is maintained at 1200 mm during the entire test. The plate is connected with a runner through a bearing. Rotating the runner moves the baffle backward, resulting in insufficient support force and active instability of the excavation face. In order to study the influence of buried depth on the stability of excavation face, three conditions of buried depth $H/D$ = 2, 1.5 and 1 are used for test, where $H$ is the thickness of soil cover

and $D$ is the diameter of tunnel. Under the three burial depth conditions, the distance of water level above the surface is defined as $H_w$. The thickness of slightly dense sandy pebble, medium dense sandy pebble and dense sandy pebble are defined as $H_1$, $H_2$ and $H_3$, respectively. Among them, the thickness ratio between the slightly dense sandy pebble and the medium dense sandy pebble is 1:1.5, and the thickness of various strata is shown in Table 2.

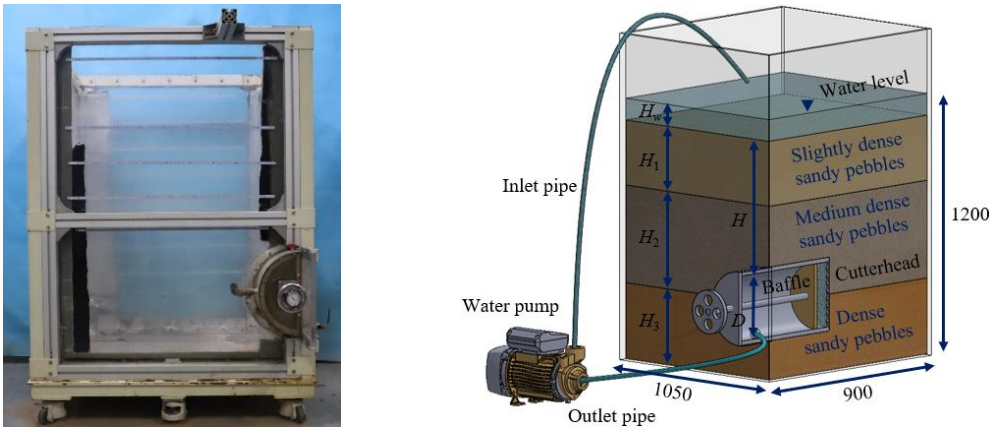


(a) Physical drawing of model box (b) Diagrammatic drawing of model box

**Fig. 2.** The tunnel excavation stability indoor model test device. Unit: mm

**Table 2.** The thickness of each stratum for various burial depths. Unit: mm

| Test condition | $H_w$ | $H_1$ | $H_2$ | $H_3$ |
|---|---|---|---|---|
| $H/D = 2$ | 100 | 300 | 450 | 350 |
| $H/D = 1.5$ | 250 | 240 | 360 | 350 |
| $H/D = 1$ | 400 | 180 | 270 | 350 |

### 3.2 Test materials and procedures

In the model tests, the soil is graded soil and prepared according to the law of similarity (Li et al. 2025). The internal friction angles for the three soils are obtained from straight shear tests. The relative compactness $D_r$ of slightly dense sandy pebble, medium dense sandy pebble and dense sandy pebble are 0.35, 0.55 and 0.75, respectively.

The test process is shown in Fig. 3, and the specific test steps are as follows:

(1) Clean the model box. Apply vaseline to the side walls of the model box to reduce the friction between the soil particles and the side walls.

(2) Carry out soil filling and leveling. According to the $D_r$ of the three strata, the filling quality of each is calculated. During the filling process, the earth pressure boxes and osmometers are buried in the designed position, and the strata is saturated with water. When the soil is filled to a height of 350 mm, lay a strip of colored sand. And

starting from 500 mm, every 100 mm lay a strip of colored sand. Colored sand is used to observe the displacement in the strata during the test. When the height of the strata reaches the predetermined position, the surface is leveled.

(3) Connect the data acquisition device. The surface displacement meters are set up on the surface, and the static strain collector and osmotic collector are connected. The static strain collector obtains the surface settlement data and earth pressure data, and the osmometer collector obtains the water pressure data.

(4) Conduct the tests. Turn the runner counterclockwise to move the baffle backward at the speed of about 1 mm/s. DIC instrument is used to monitor strain and displacement of the strata throughout the test. The test is finished when the baffle has moved 10 cm.

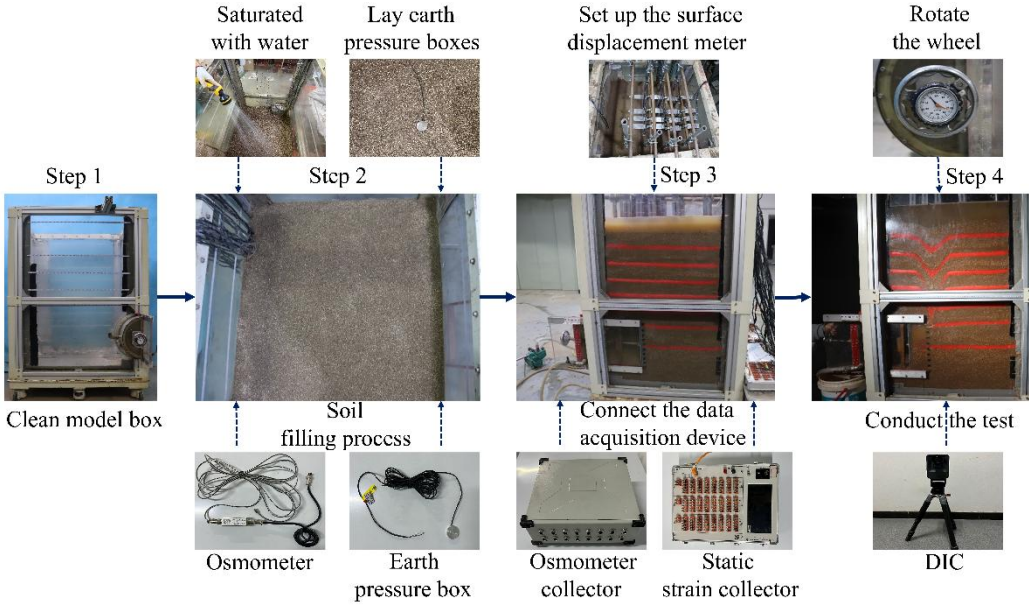


**Fig. 3.** Test process.

### 3.3 Monitoring point arrangement

As shown in Fig. 4, 16 surface displacement monitoring points have been arranged on the strata surface to monitor changes in surface settlement.

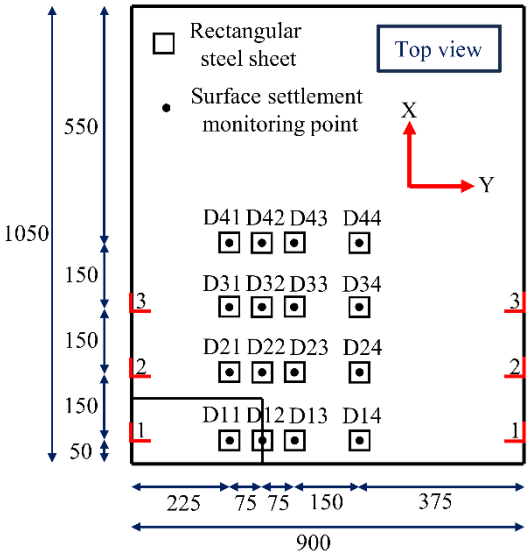


**Fig. 4.** Distribution of surface settlement monitoring points. Unit: mm

When H/D = 2 and H/D = 1.5, the arrangement of vertical soil pressure boxes is shown in Fig. 5, with a total of 23 earth pressure boxes. When *H*/*D* = 1, the vertical earth pressure boxes in the strata are arranged as shown in Fig. 6. There are 16 earth pressure boxes in total, which are used to monitor the change law of earth pressure in the strata.

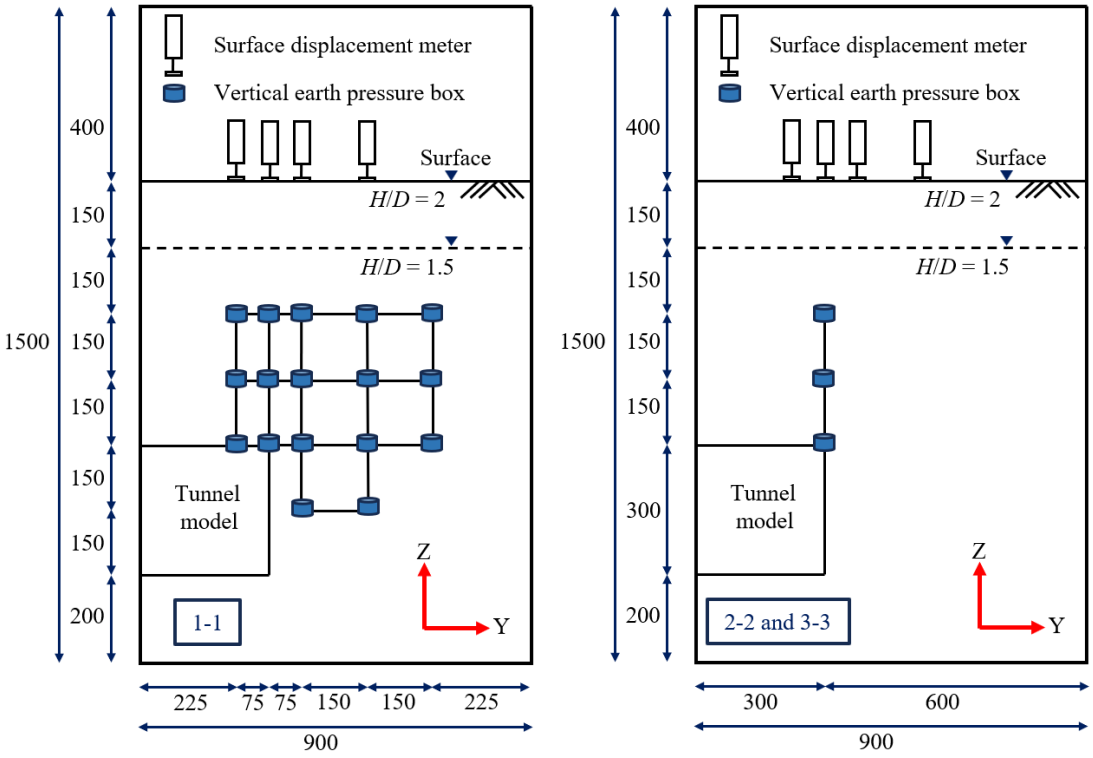


(a) 1-1 section (b) 2-2 and 3-3 section

**Fig. 5.** Distribution of earth pressure boxes in the strata for *H*/*D* = 2 and *H*/*D* = 1.5. Unit: mm

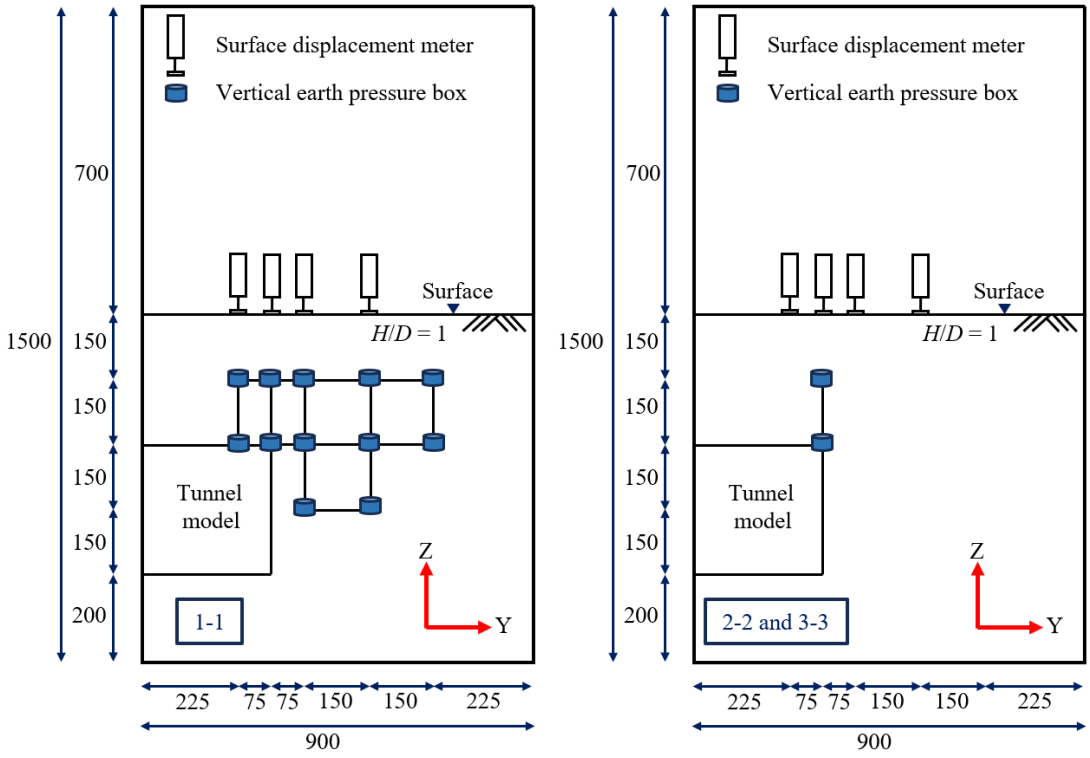


(a) 1-1 section (b) 2-2 and 3-3 section

**Fig. 6.** Distribution of earth pressure boxes in the strata for $H/D = 1$. Unit: mm

6 earth pressure boxes and 4 osmometers are dispersed on the cutterhead, while 5 osmometers are dispersed on the side wall of the model box in front of the excavation face. The arrangement of earth pressure boxes and osmometers are shown in Fig. 7.

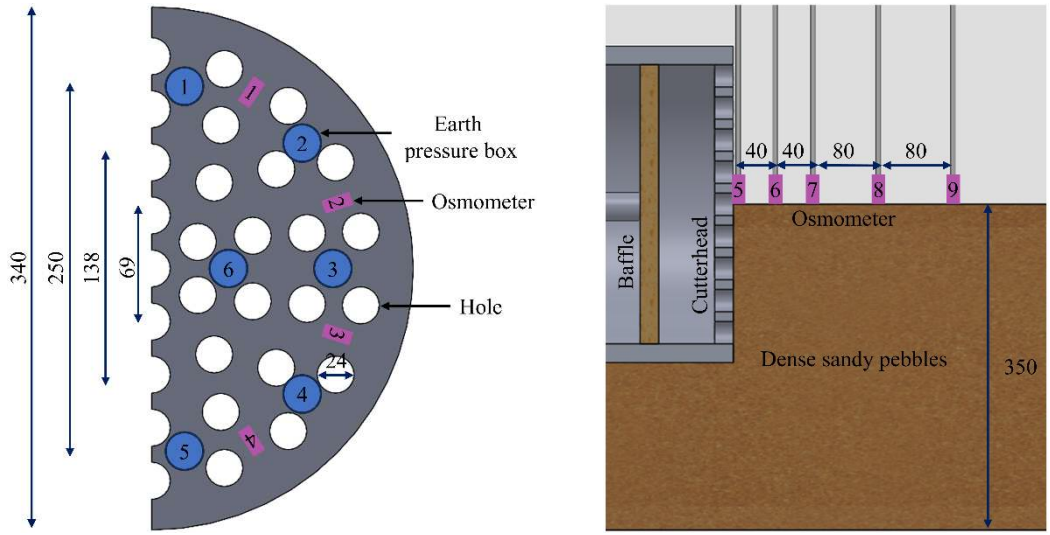


(a) Instrument layout on the cutterhead (b) Osmometers in front of excavation face

**Fig. 7.** The arrangement of earth pressure boxes and osmometers. Unit: mm

### 3.4 Numerical model establishment

Table 2 also shows the thickness of the three strata under various burial depths, as established using ABAQUS software. The soil permeability coefficient $k = 2 \times 10^{-5}$ m/s,

which is obtained from the constant head permeability test, is used in the numerical simulations.

The steps of numerical simulation are as follows:

(1) A numerical model corresponding to the model test dimensions was established based on the corresponding burial depth, as shown in Fig. 8. The tunnel is partially empty and the lining unit supports it. The material's properties are essentially consistent with those of the soil in the model tests. After setting the corresponding boundary conditions, the geo-stress balance is carried out.

(2) The excavation face moves backwards at a rate of 0.002 mm each time and fluid-structure coupling calculations are performed.

(3) For each 1 mm movement, the excavation face's restriction condition is converted to a normal fixed restriction, and the fluid-structure coupling computation is then repeated until the equilibrium state is reached. The numerical simulation is finished when the movement distance reaches 10 cm.

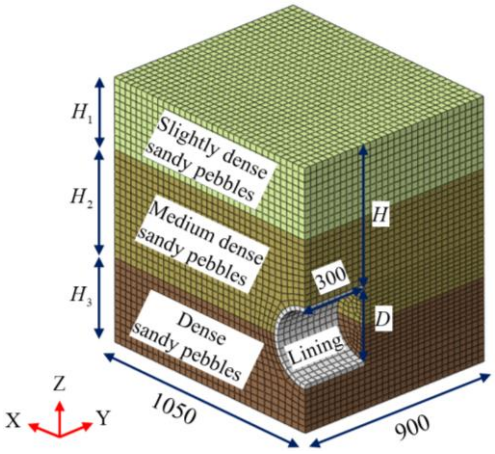


**Fig. 8.** Numerical model. Unit: mm

## 4 Test results analysis

### 4.1 Surface settlement analysis and soil arch development

The change process of the soil displacement increment field at various burial depths is acquired by the analysis of the DIC instrument, as illustrated in Figs. 9–11. Points A, B, and C, respectively, are the places where the highest displacement of ground settlement occurs under three distinct burial depth environments.

There are three stages to the peak displacement change process, regardless of whether they are model tests or numerical simulations. Figs. 12–14 display the peak displacement change law with $L$. Under different burial depths, the corresponding

ranges of $L$ in the three stages are shown in Table 3.

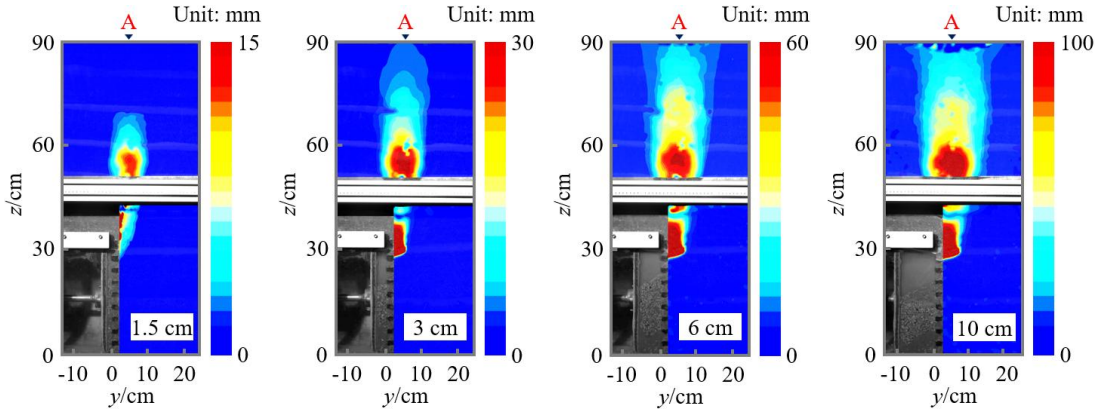


**Fig. 9.** The change law of displacement increment field with $L$ for $H/D$ = 2.

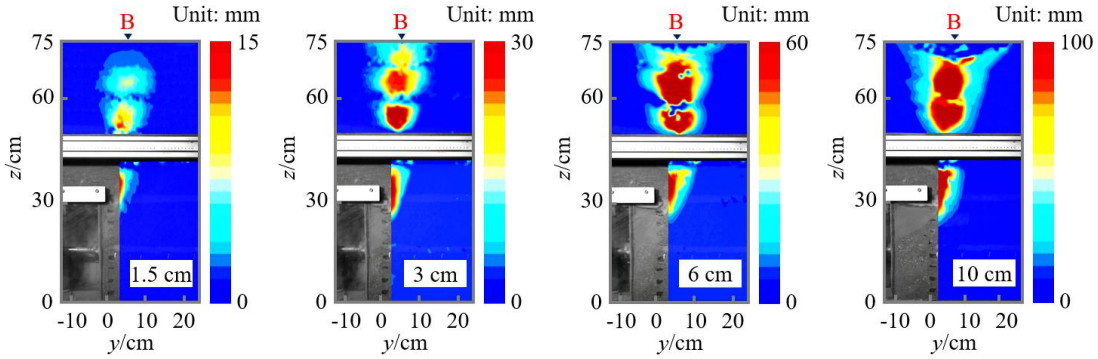


**Fig. 10.** The change law of displacement increment field with $L$ for $H/D$ = 1.5.

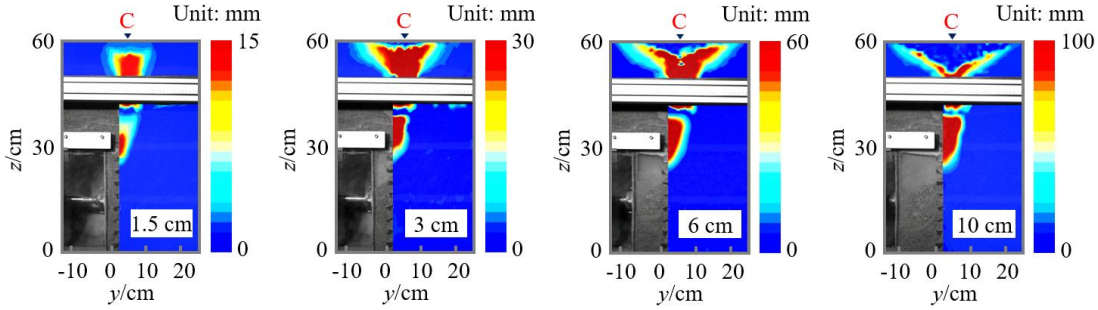


**Fig. 11.** The change law of displacement increment field with $L$ for $H/D$ = 1.

**Table 3.** The range of $L$ in each stage for various burial depths.

| Test condition | | $L$ (cm) | | |
|---|---|---|---|---|
| | | First phase | Second phase | Third phase |
| Model test | $H/D$ = 2 | 0-2 | 2-3.5 | 3.5-10 |
| | $H/D$ = 1.5 | 0-1.6 | 1.6-2.5 | 2.5-10 |
| | $H/D$ = 1 | 0-1.3 | 1.3-1.9 | 1.9-10 |
| Numerical simulation | $H/D$ = 2 | 0-2.2 | 2.2-4 | 4-10 |
| | $H/D$ = 1.5 | 0-2 | 2-3.1 | 3.1-10 |
| | $H/D$ = 1 | 0-1.5 | 1.5-2.4 | 2.4-10 |

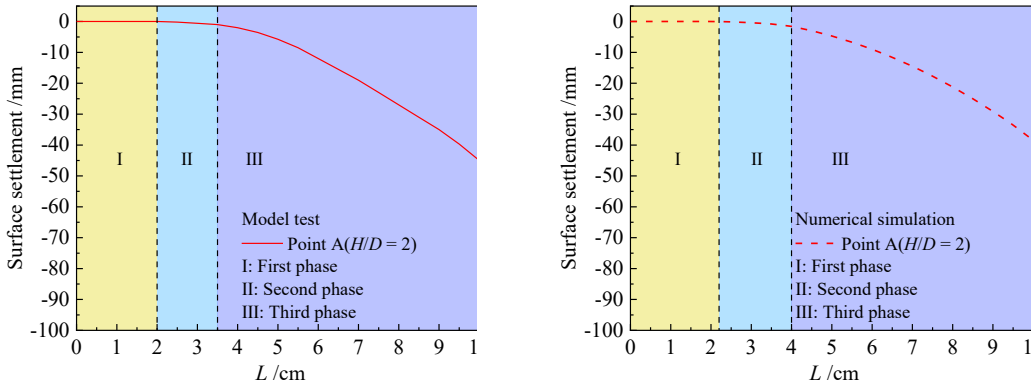


(a) Model test (b) Numerical simulation

**Fig. 12.** The change law of peak displacement of surface settlement with $L$ for $H/D$ = 2.

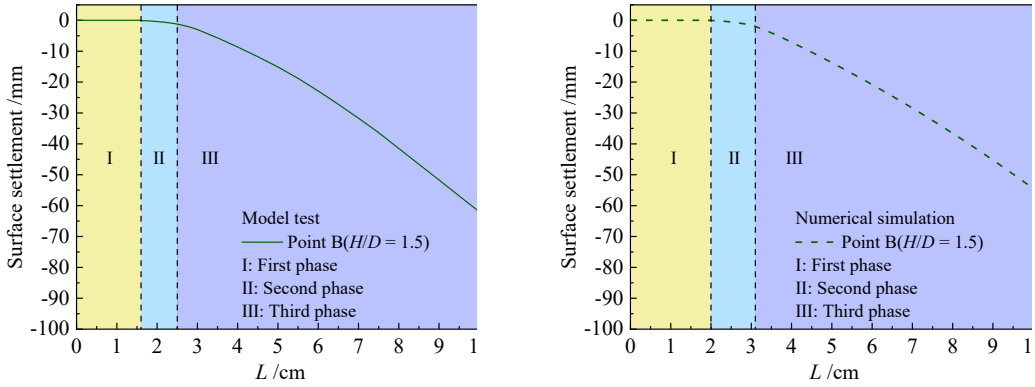


(a) Model test (b) Numerical simulation

**Fig. 13.** The change law of peak displacement of surface settlement with $L$ for $H/D$ = 1.5.

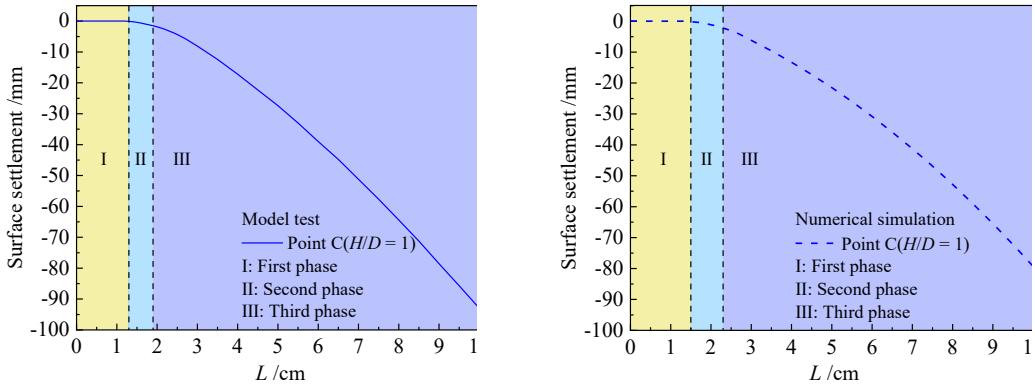


(a) Model test (b) Numerical simulation

**Fig. 14.** The change law of peak displacement of surface settlement with $L$ for $H/D$ = 1.

(1) No settlement stage. The soil ahead of the excavation face experiences active instability as a result of the increase in L. Meanwhile, the soil arch effect begins to form and gradually develop in the strata. However, the soil arch has not yet developed to the surface, so the surface has not settled at this stage.

(2) Slow settlement stage. As $L$ continues to increase, the soil arch effect develops to the surface. However, at this stage, the instability range of the stratum is mainly

increased, so slow settlement occurs at the surface.

(3) Rapid settlement stage. As the soil arch effect gradually fades, the strata become generally unstable, and settlement spreads quickly.

Meanwhile, with the decrease of burial depth, the peak displacement increases gradually under the same $L$. In addition, under the same conditions, the settlement values of numerical simulations are smaller than that of model tests. This is because the soil material in numerical simulations is based on the assumption of continuous media, while the soil material in model tests is relatively discrete and has discontinuity, resulting in large surface settlement obtained in model tests.

### 4.2 Three-dimensional surface settlement analysis

Figs. 15–17 show the deformation results of the strata under different burial depths when $L$ = 10 cm. Under different burial depth conditions, three-dimensional surface settlement is shown in Fig. 18.

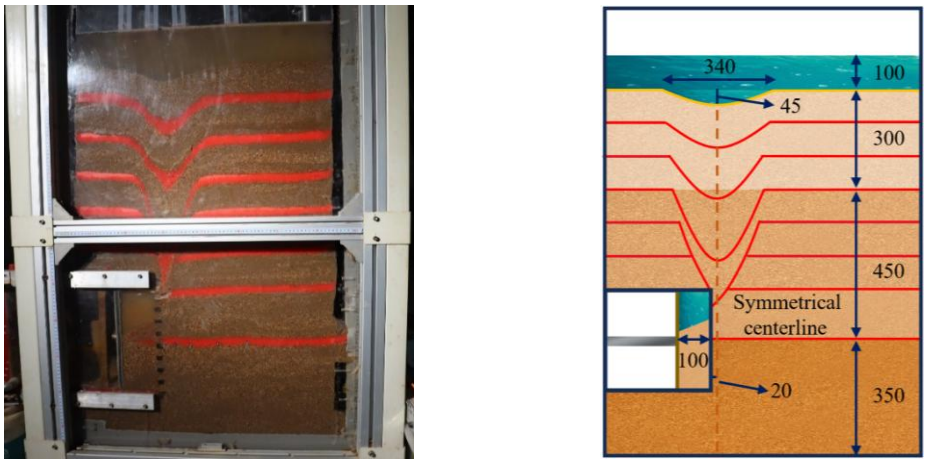


(a) Physical drawing (b) Diagrammatic drawing

**Fig. 15.** The deformation result of the strata for $H/D$ = 2. Unit: mm

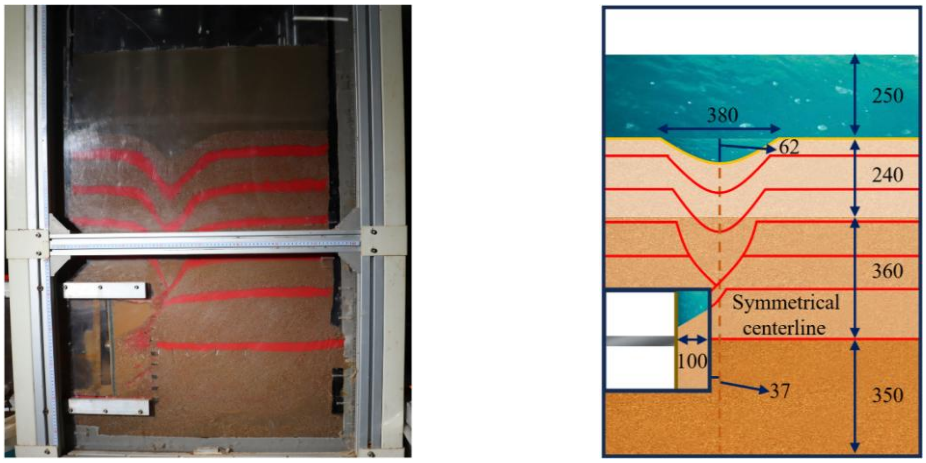


(a) Physical drawing (b) Diagrammatic drawing

**Fig. 16.** The deformation result of the strata for $H/D$ = 1.5. Unit: mm

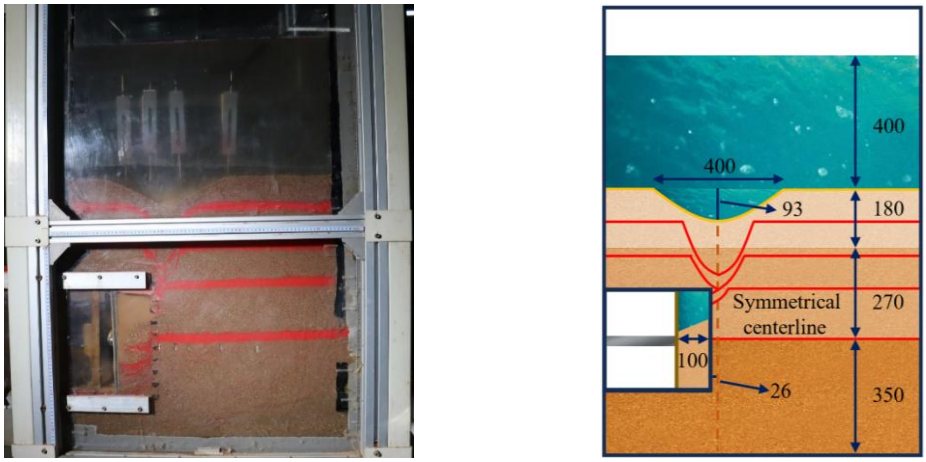


(a) Physical drawing (b) Diagrammatic drawing

**Fig. 17.** The deformation result of the strata for $H/D$ = 1. Unit: mm

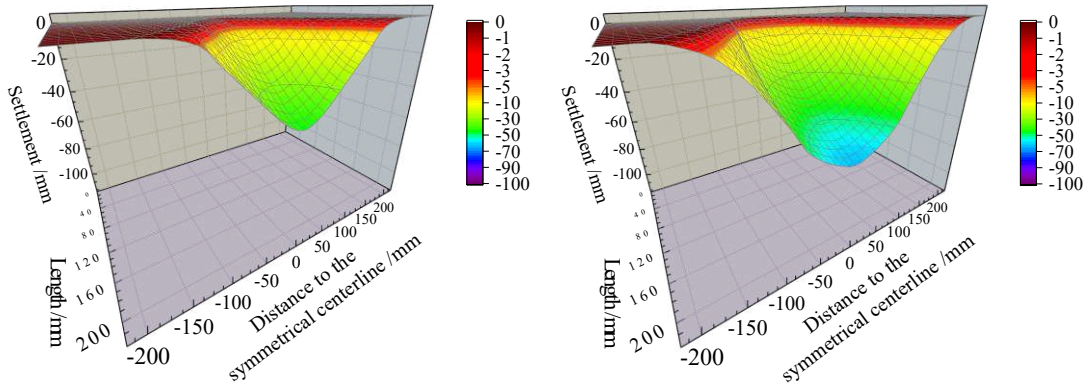


(a) $H/D$ = 2 (b) $H/D$ = 1.5

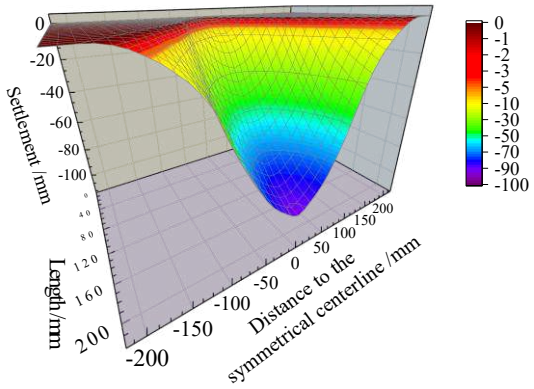


(c) $H/D$ = 1

**Fig. 18.** Three-dimensional surface settlement for various burial depths.

When $L$ = 10 cm, the surface creates a semi-funnel-shaped settlement area. The settlement funnel's symmetrical centerlines are situated ahead of the digging face, and it is 20 mm, 37 mm, and 26 mm away from the digging face at various buried depths. The diameter of the settlement funnel progressively increases to 34 cm (1.13$D$), 38 cm

(1.27$D$), and 40 cm (1.33$D$) as the buried depth decreases. The maximum settlement values are also gradually increasing, with values of 45 mm, 62 mm and 93 mm, respectively.

### 4.3 Seepage field analysis

Figs. 19–21 illustrate the changing rule of pressure in water with $L$ at various burial depth settings. It is evident that each osmometer's water pressure exhibits a propensity to rise and then stabilize as L increases. In addition, the increase of water pressure of osmometer 9 furthest away from the excavation surface is relatively small. This shows that the seepage path range of water is basically same under different burial depths. Osmometers on the cutterhead and osmometers 5, 6, and 7 close to the excavation face show an increase in water pressure as the burial depth decreases. This shows that the decrease of the burial depth will increase the water seepage velocity.

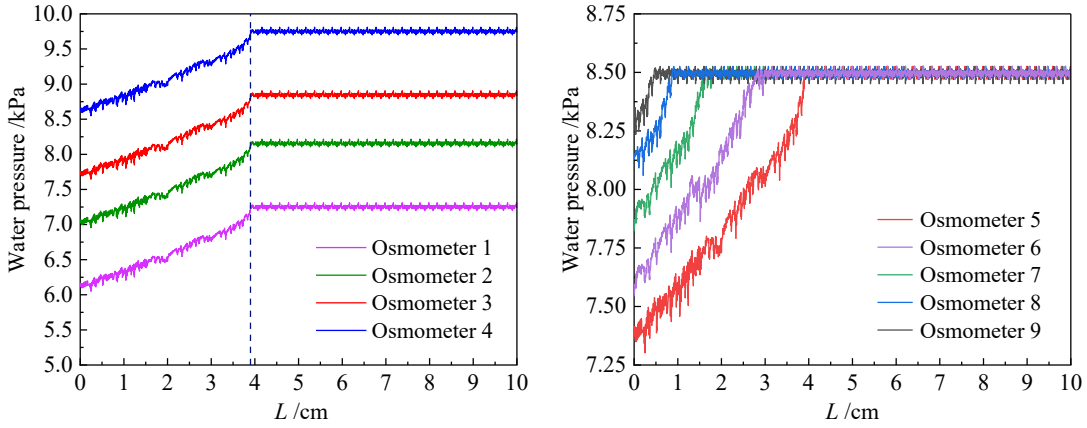


(a) Water pressure on excavation face (b) Water pressure in front of excavation face

**Fig. 19.** The change law of water pressure with $L$ for $H/D$ = 2.

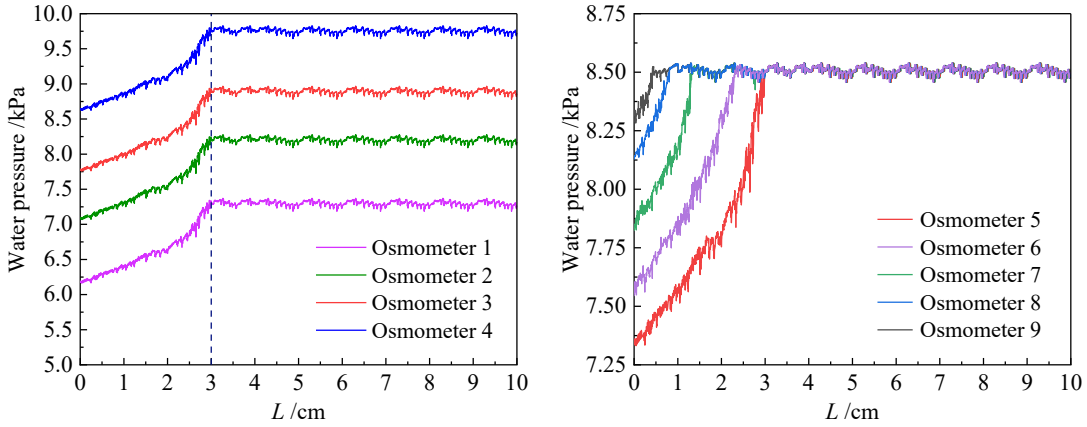


(a) Water pressure on excavation face (b) Water pressure in front of excavation face

**Fig. 20.** The change law of water pressure with $L$ for $H/D$ = 1.5.

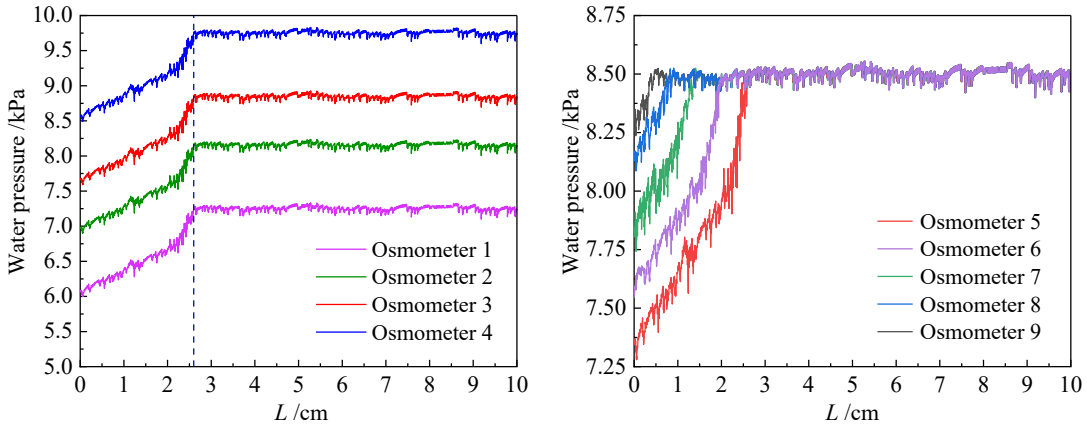


(a) Water pressure on excavation face (b) Water pressure in front of excavation face

**Fig. 21.** The change law of water pressure with $L$ for $H/D$ = 1.

In order to verify the above conclusions, the numerical simulation method is used for further analysis. The pore pressure distribution and seepage velocity of strata under different burial depths are shown in Figs. 22–24. While the far boundary continues to maintain hydrostatic pressure, ground water flows in the direction of the excavated area. Under different burial depth conditions, the scope of water seepage pathways is about 0-0.72$D$, and this shows that the decrease of burial depth has essentially no effect on the seepage path range of water.

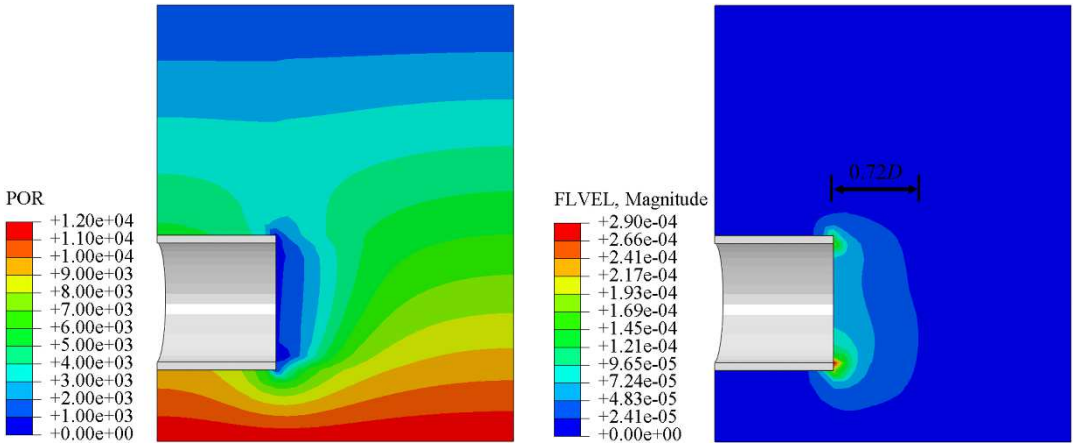


(a) Pore pressure distribution (b) Seepage velocity

**Fig. 22.** The pore pressure distribution and seepage velocity of strata for $H/D$ = 2.

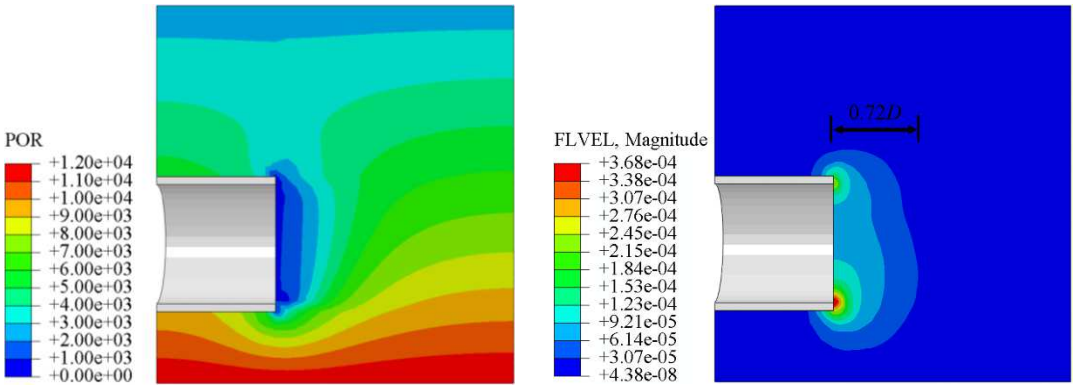


(a) Pore pressure distribution (b) Seepage velocity

**Fig. 23.** The pore pressure distribution and seepage velocity of strata for $H/D$ = 1.5.

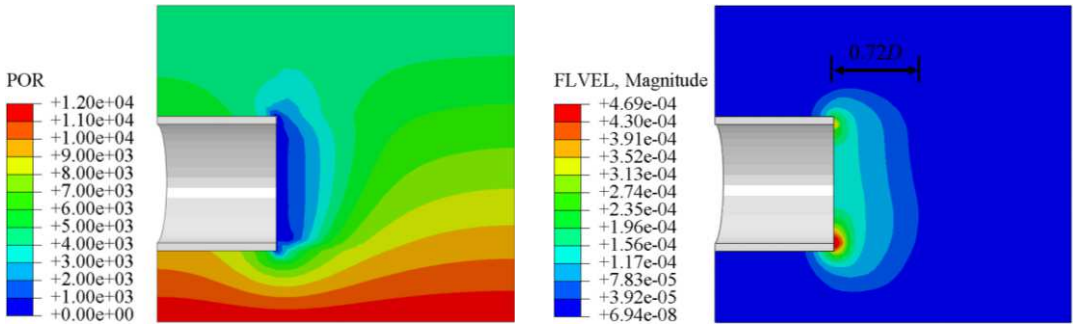


(a) Pore pressure distribution (b) Seepage velocity

**Fig. 24.** The pore pressure distribution and seepage velocity of strata for $H/D$ = 1.

Fig. 25 displays the changing law of seepage velocity on the excavated face along the diameter direction. Under different burial depths, the seepage velocity shows a tendency to decrease and then increase along the diameter of the excavated face. With z between 0 and 10 cm (0 and $D/3$), the seepage velocity progressively drops. With z between 10 and 30 cm ($D/3$-$D$), the seepage velocity progressively rises. At the base of the excavated face, the seepage velocity is at its highest. This is because water flows from the area of high water pressure to the area of low water pressure, and the water pressure difference at the bottom of the excavation face is the largest, and the seepage velocity is the largest. And at the same $z$, the seepage velocity increases gradually with the decrease of burial depth. When the buried depth $H/D$ = 2, 1.5 and 1, the maximum seepage velocity is $2.90\times10^{-4}$ m/s, $3.68\times10^{-4}$ m/s and $4.69\times10^{-4}$ m/s, respectively. This is because as buried depth increases, earth obstruction to water flow increases, slowing down the water's seepage velocity. The conclusion drawn from the model tests is in line with this.

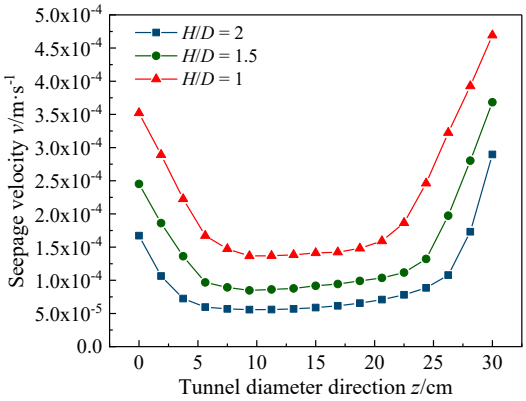


**Fig. 25.** The Seepage velocity of excavation face for various burial depths.

## 4.4 Limit equilibrium state analysis of strata

Fig. 26 illustrates the changing rule of soil pressure on the cutterhead with L at various buried depths.

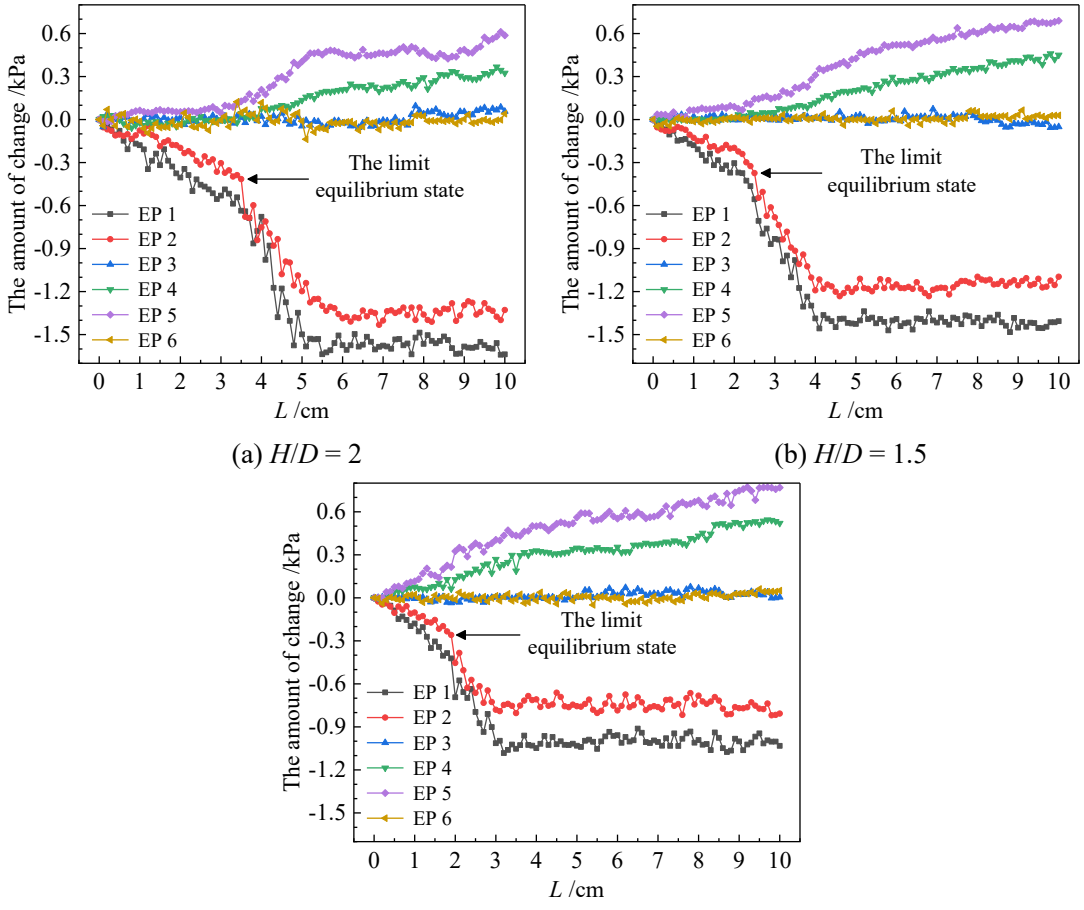


(a) $H/D = 2$ (b) $H/D = 1.5$

(c) $H/D = 1$

**Fig. 26.** The change law of earth pressure on cutterhead with $L$ for various burial depths.

Under various buried depth circumstances, the values of EP 3 and EP 6 fixed at the center of the excavated face are essentially steady. The soil particles in the stratum enter the chamber through the opening hole in the upper portion of the cutterhead as

the baffle slides backwards during the whole test. Therefore, the instability of dense sandy pebble stratum has not been occurred. In Figs. 15–17, the colored sand at 350 mm always maintains a straight line, which can also verify this conclusion.

In the lower portion of the excavation face, the values of EP 4 and EP 5 increase as $L$ increases. Due to the increasing of soil particles entering the chamber, the horizontal extrusion pressure acting on the lower part of cutterhead increases. When $L$ = 10 cm, with the decrease of buried depth, the increase amounts of EP 5 is 0.59 kPa, 0.69 kPa and 0.77 kPa, respectively. This suggests that the collapsed area over the excavation face will expand as the buried depth decreases and the chamber's soil intake increases.

The values of EP 4 and EP 5 fixed in the upper part of the excavation face shows a trend of slow decline at first, then rapid decline and finally stability. The soil primarily enters the soil bin through the opening hole in the top portion of the cutter head due to the baffle's movement, which causes the values of EP 1 and EP 2 to gradually decrease. The limit equilibrium state of the strata will be broken and there will be general instability as $L$ increases steadily. A small disturbance will cause a large amount of soils to collapse, resulting in a rapid decrease in earth pressure. The comparable $L$ values in the limit state of equilibrium are 3.5 cm, 2.5 cm, and 1.9 cm, respectively, for $H/D$ = 2, 1.5, and 1. This suggests that lowering the burial depth will cause the strata's limit equilibrium condition to be broken more quickly, causing the strata to become unstable overall sooner rather than later.4.5 Instability pattern analysis of strata

Under the geological conditions where strata are loose, saturated or has other unstable characteristics, there is a close relationship between the variation area of earth pressure and the instability range of strata. The definition of $n_{sx}$ is a proportion of the vertical soil pressure box's soil pressure value under various L to its original value. The change law of $n_{sx}$ along and perpendicular to tunnel direction are shown in Figs. 27–29. The $n_{sx}$ in the change range is always less than 1 and progressively gets smaller as L increases under the same burial depth condition. And the closer the earth pressure box is to the excavation face, the smaller the $n_{sx}$ is. In the meantime, the variation area of earth pressure under the same $L$ progressively expands as the buried depth drops, and the $n_{sx}$ at the same place in the variation area gradually decreases. This demonstrates how lowering the burial depth will raise the variation area and disturbed degree of earth pressure, which will in turn raise the range and degree of instability of the strata. In

addition, when $L$ is equal, the $n_{sx}$ in front of the excavated face is less than the nsx behind it. The degree of instability in front of the excavation face is higher than that behind it, as demonstrated by this.

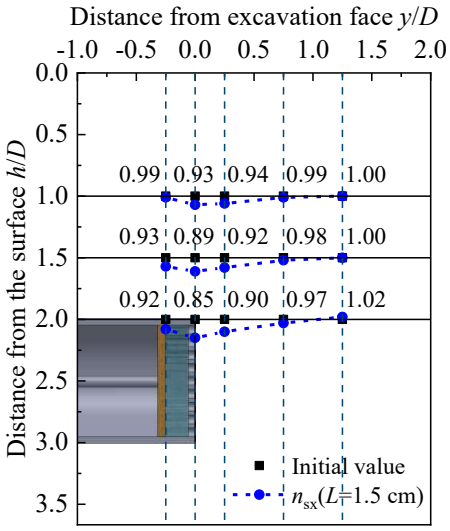


(a) $n_{sx}$ along tunnel for $L$ = 1.5 cm

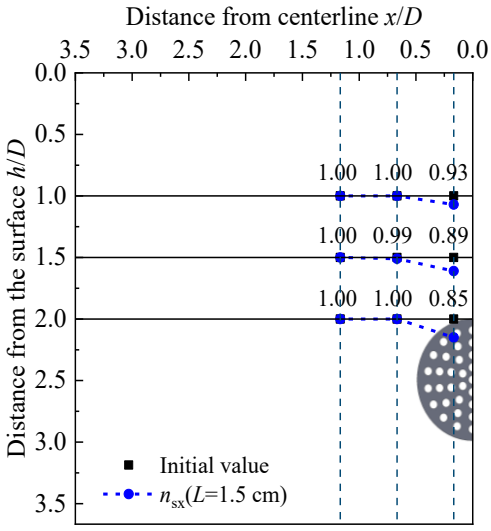


(b) $n_{sx}$ perpendicular to tunnel for $L$ = 1.5 cm

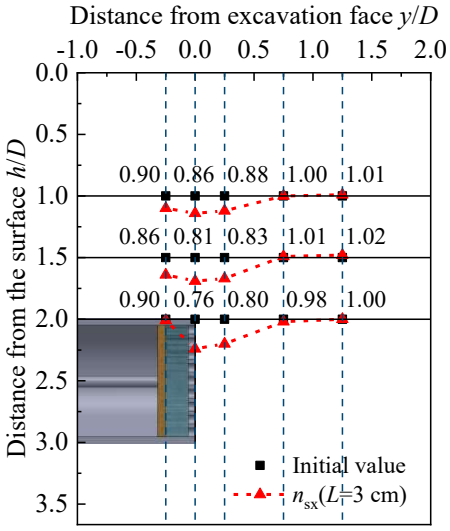


(c) $n_{sx}$ along tunnel for $L$ = 3 cm

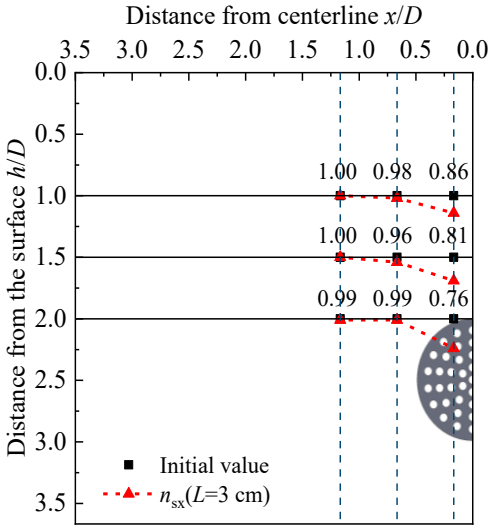


(d) $n_{sx}$ perpendicular to tunnel for $L$ = 3 cm

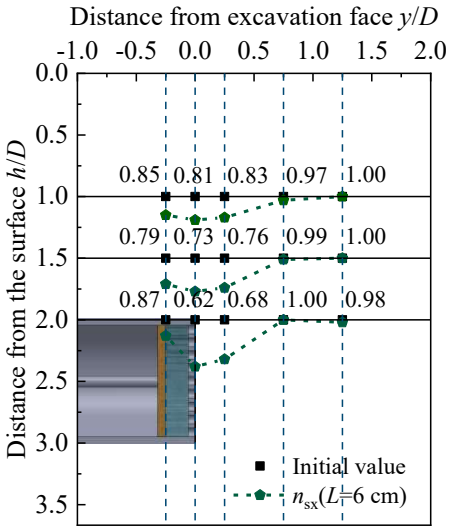


(e) $n_{sx}$ along tunnel for $L$ = 6 cm

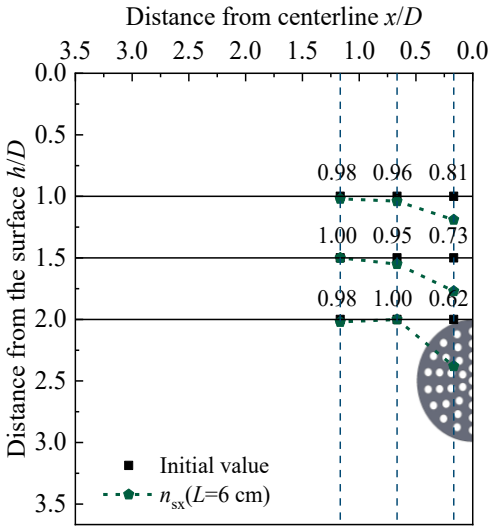


(f) $n_{sx}$ perpendicular to tunnel for $L$ = 6 cm

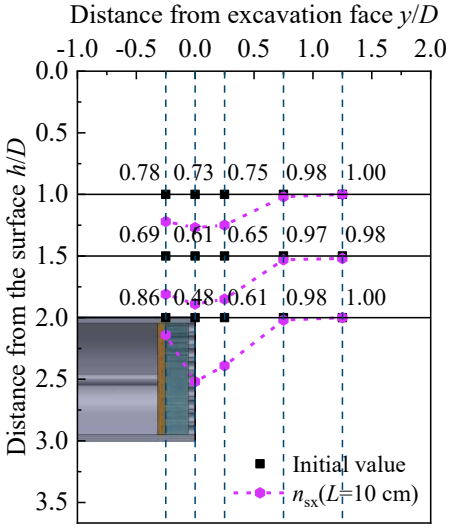


(g) $n_{sx}$ along tunnel for $L$ = 10 cm

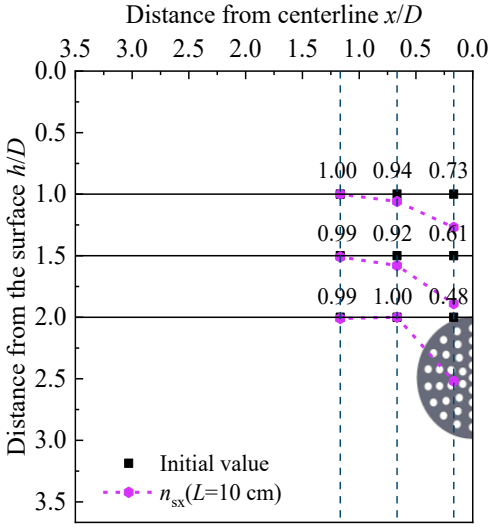


(h) $n_{sx}$ perpendicular to tunnel for $L$ = 10 cm

**Fig. 27.** The change law of $n_{sx}$ with $L$ for $H/D$ = 2.

300

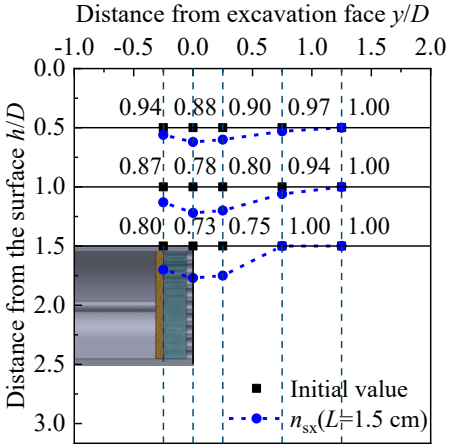


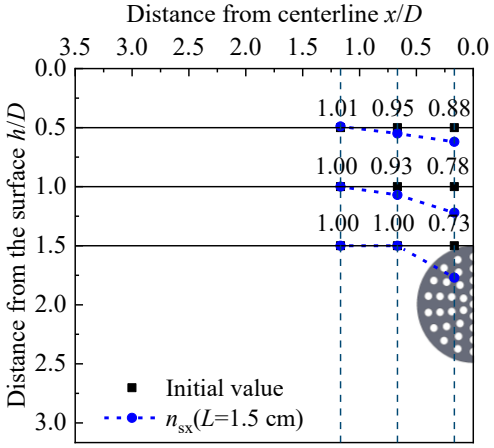

(a) $n_{sx}$ along tunnel for $L$ = 1.5 cm

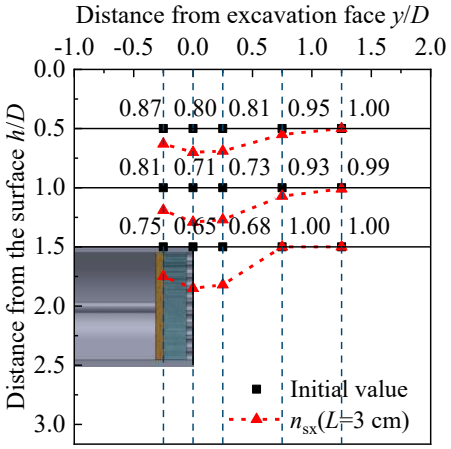


(b) $n_{sx}$ perpendicular to tunnel for $L$ = 1.5 cm

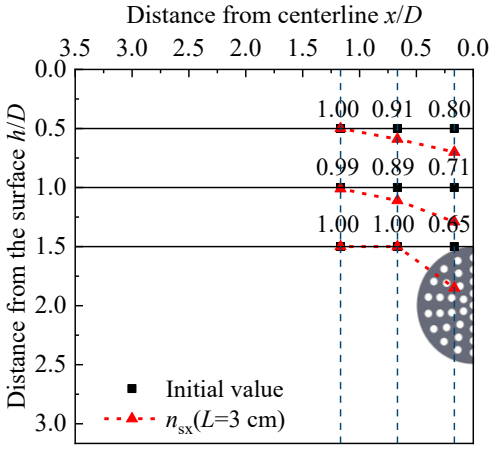


(c) $n_{sx}$ along tunnel for $L$ = 3 cm

(d) $n_{sx}$ perpendicular to tunnel for $L$ = 3 cm

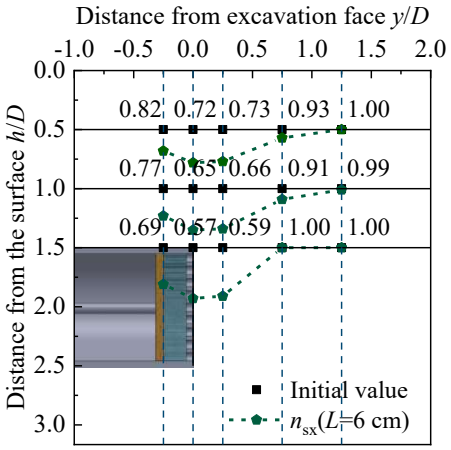


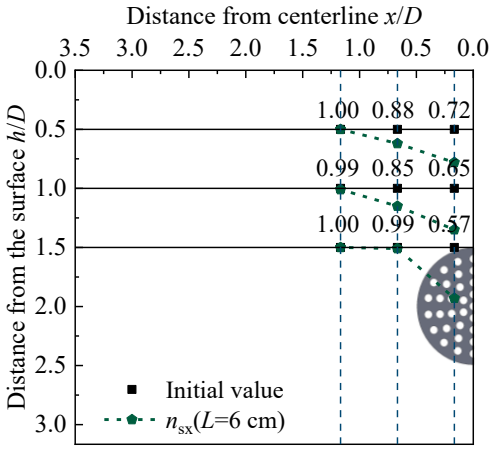


(e) $n_{sx}$ along tunnel for $L$ = 6 cm

(f) $n_{sx}$ perpendicular to tunnel for $L$ = 6 cm

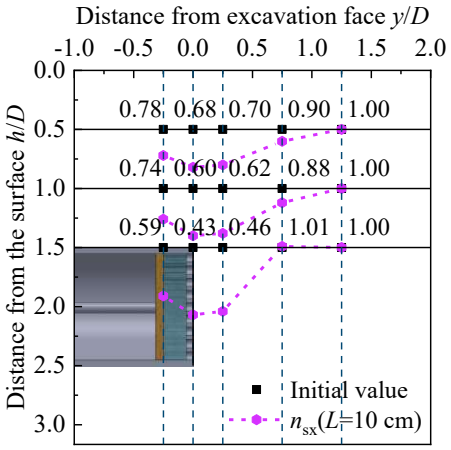


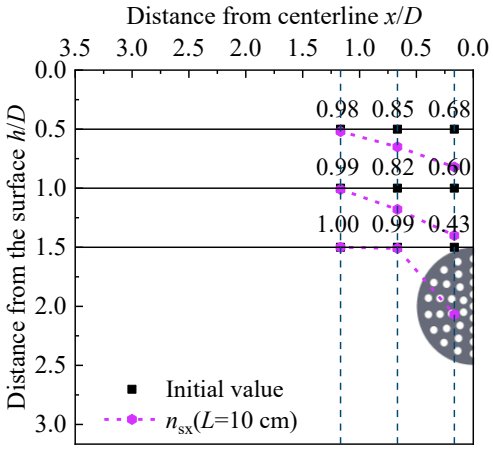


(g) $n_{sx}$ along tunnel for $L$ = 10 cm

(h) $n_{sx}$ perpendicular to tunnel for $L$ = 10 cm

**Fig. 28.** The change law of $n_{sx}$ with $L$ for $H/D$ = 1.5.

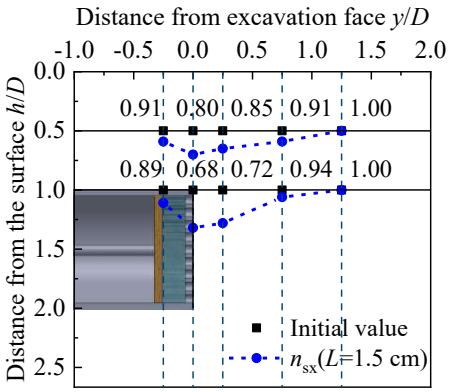


(a) $n_{sx}$ along tunnel for $L$ = 1.5 cm

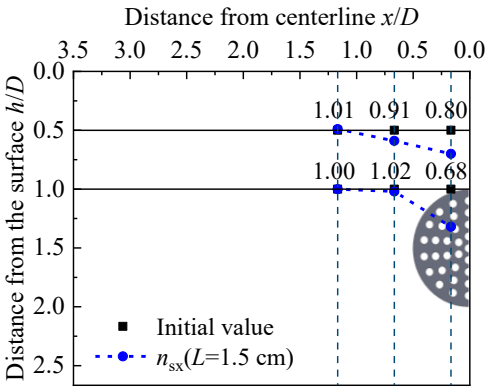


(b) $n_{sx}$ perpendicular to tunnel for $L$ = 1.5 cm

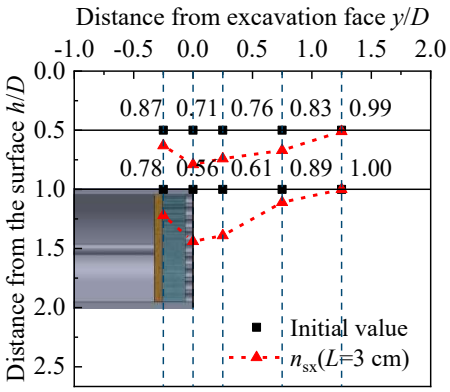


(c) $n_{sx}$ along tunnel for $L$ = 3 cm

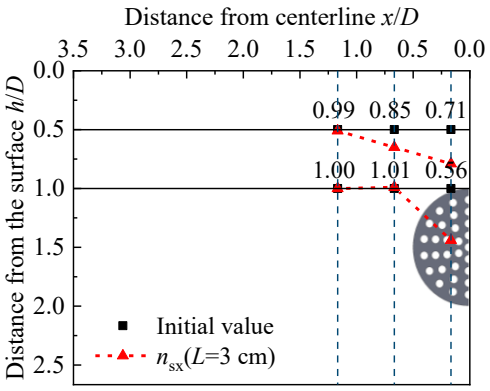


(d) $n_{sx}$ perpendicular to tunnel for $L$ = 3 cm

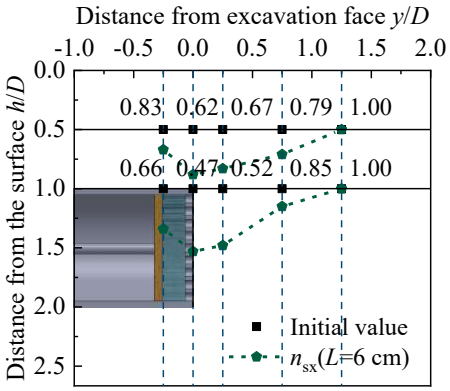


(e) $n_{sx}$ along tunnel for $L$ = 6 cm

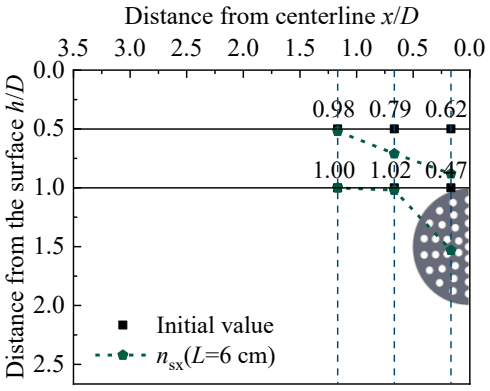


(f) $n_{sx}$ perpendicular to tunnel for $L$ = 6 cm

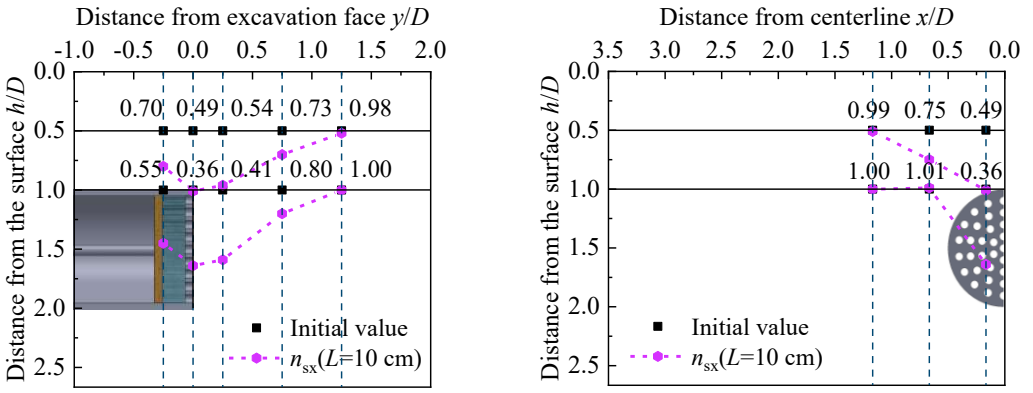


(g) $n_{sx}$ along tunnel for $L$ = 10 cm (h) $n_{sx}$ perpendicular to tunnel for $L$ = 10 cm

**Fig. 29.** The change law of $n_{sx}$ with $L$ for $H/D$ = 1.

Under different burial depth conditions, the displacement increment field obtained by DIC is also the instability range of the strata, as shown in Figs. 30–32. It can be seen that in the strata with lower dense and upper loose, the instability failure is distributed in the middle-upper part of the excavation face. The loose stratum in the higher part primarily controls the strata's deformation and collapse, while the dense sandy pebble layer maintains its stability. At the same time, as $L$ rises under various burial depths, the strata's unstable area grows. When the baffle begins to move backwards, the soil arch forms and gradually develops. If the unstable area is abstracted into geometry, and the unstable area of the stratum is the model of "quarter ellipsoid + circular table + half ellipsoid" in this phase. The "quarter ellipsoid + double circular table" model of excavation face instability is created when the soil arch effect fails, resulting in general stratum unstable.

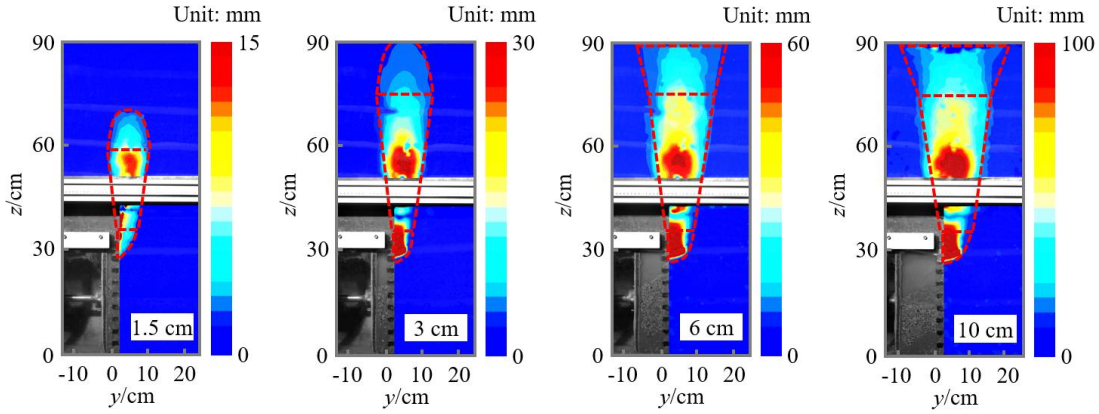


**Fig. 30.** The change law of instability range with $L$ for $H/D$ = 2.

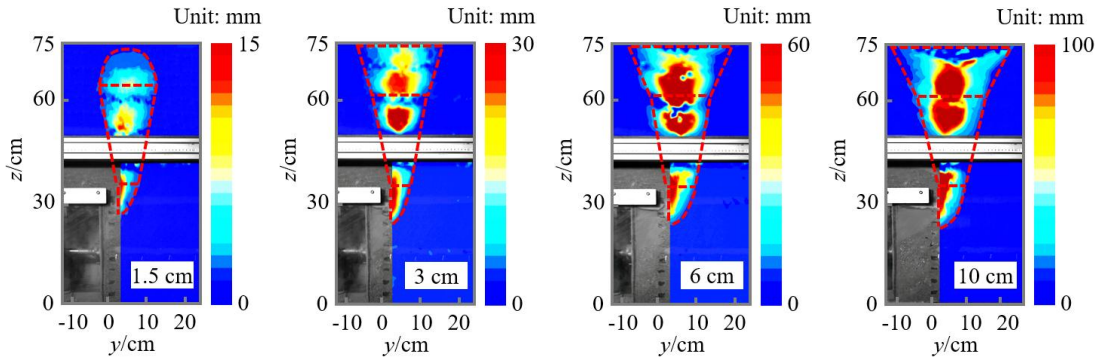


**Fig. 31.** The change law of instability range with $L$ for $H/D$ = 1.5.

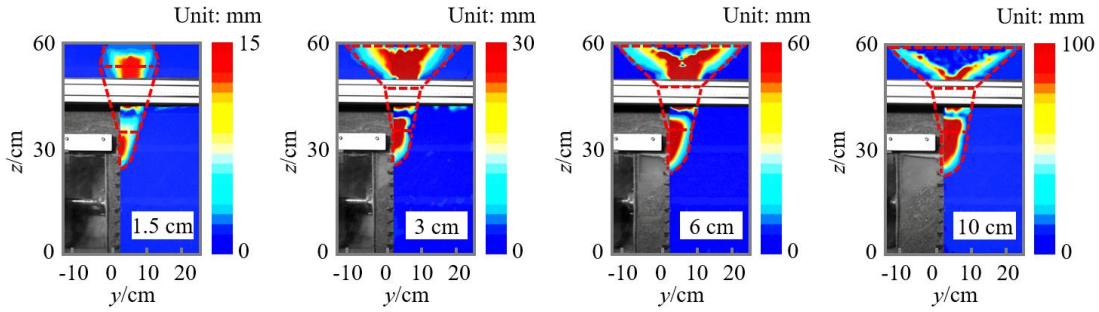


**Fig. 32.** The change law of instability range with $L$ for $H/D$ = 1.

In order to further analyze the characteristics of this strata, numerical simulations are used to compare it with the homogeneous medium dense sandy pebble strata whose relative compactness $D_r$ is 0.55. The unstable range of the two layers under various burial depths, as determined by numerical simulations, is displayed in Figs. 33–35 when $L$ = 10 cm. According to the results of model studies, the upper portion of the region exhibits the greatest displacement of the excavation face in the upper loose and lower compact layers. However, the maximum displacement of the excavation face in the homogeneous sandy pebble strata occurs in the middle region. Because the upper stratum in the lower dense and upper loose stratum is loose and has a low shear strength, the upper portion of the excavated face destabilizes more readily. The unstable area of the lower dense and upper loose stratum, which are 1.06$D$, 1.22$D$, and 1.29$D$, respectively, is shown to progressively rise as the buried depth decreases. And the unstable area of the uniform stratum whose $D_r$ is 0.55 also increased gradually, which are 0.97$D$, 1.10$D$ and 1.20$D$, respectively. Lower dense and upper loose strata have a wider range of unstable than uniform stratum in identical circumstances. This is due to the discontinuity of stress transfer between loose stratum and dense stratum. When the loose stratum is unstable, the shear failure will develop along the interface, which intensifies the growth of the unstable area.

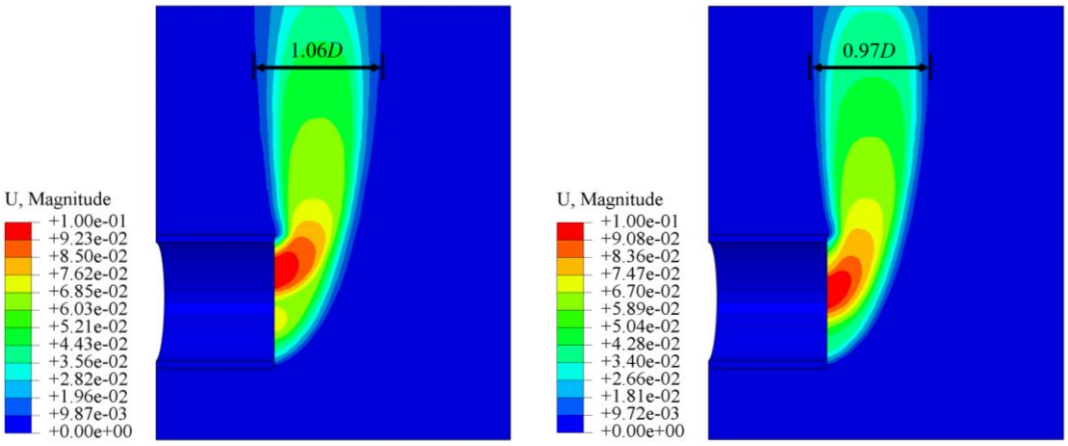


(a) The loose and lower dense strata (b) The homogeneous strata

**Fig. 33.** Comparison of instability range of two strata for $H/D = 2$.

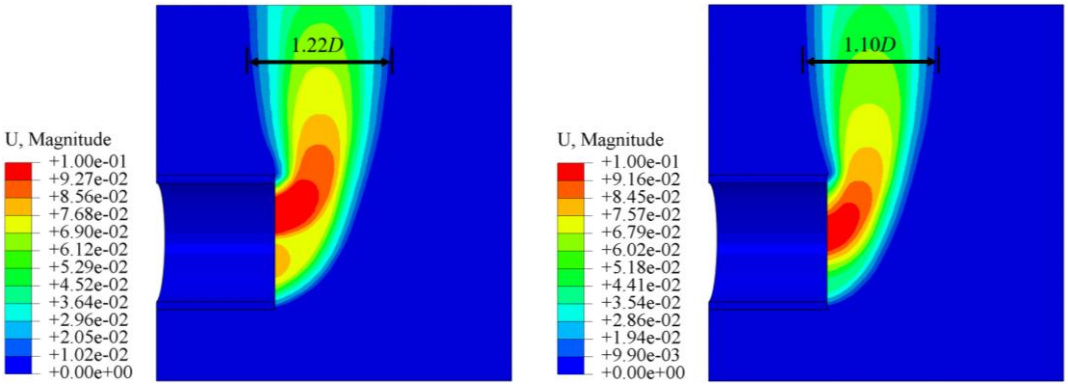


(a) The loose and lower dense strata (b) The homogeneous strata

**Fig. 34.** Comparison of instability range of two strata for $H/D = 1.5$.

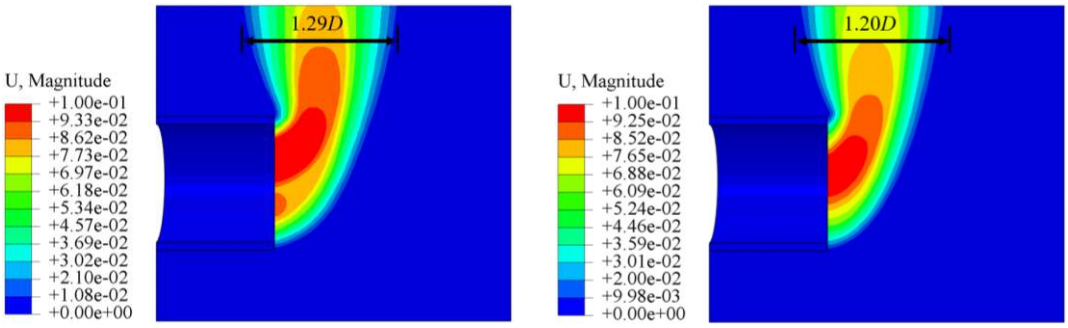


(a) The loose and lower dense strata (b) The homogeneous strata

**Fig. 35.** Comparison of instability range of two strata for $H/D = 1$.

## 5 Theoretical analysis of excavation face stability

### 5.1 Theoretical calculation model of excavation face stability

Combined with the formation instability range obtained in Figs. 30–32, the theoretical calculation model of excavation face stability is proposed, as shown in Fig. 36. In the calculation model, the soil failure zone in front of excavation is composed of circular table I, circular table II and wedge III. The distinction between medium-density

and slightly-density sandy pebbles marks the division between circular tables I and II. The boundary between circular table II and wedge III is the dividing line between medium-density and slightly-density sandy pebbles.

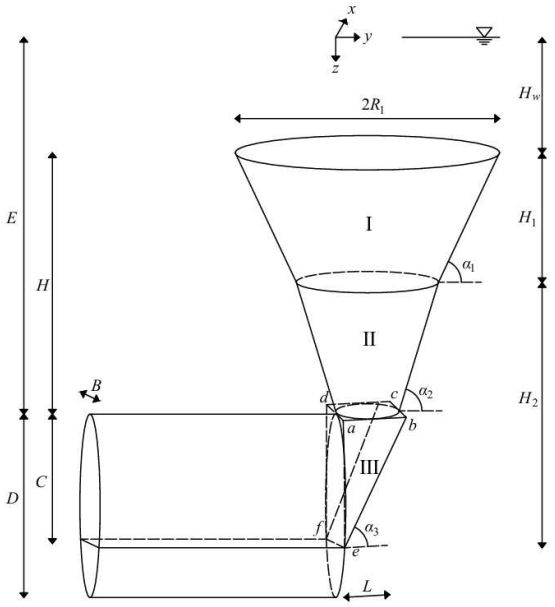


**Fig. 36.** Theoretical calculation model of excavation face stability.

Fig. 36 shows the tunnel's diameter ($D$), water level height above the tunnel top ($E$), and distance between the surface and the tunnel top ($H$). $H_1$ is the depth of slightly-density sandy pebble strata, $H_2$ is the depth of medium-density sandy pebble formation, and $H_w$ is the distance of water level above surface. $\alpha_1$ is the inclination angle of circular table I, $\alpha_1 = 45^\circ + \frac{\varphi_1}{2}$, and $\varphi_1$ is the internal friction angle of slightly dense sandy pebbles. $\alpha_2$ is the inclination angle of circular table II. $\alpha_3$ is the angle between sliding surface of wedge III and horizontal direction, $\alpha_3 = 45^\circ + \frac{\varphi_2}{2}$, and $\varphi_2$ is the internal friction angle of medium dense sandy pebbles. Points $a$, $b$, $c$, $d$, $e$ and $f$ are the vertices of wedge III respectively. Wedge III's width, height, and length are denoted by $B$, $C$, and $L$, respectively.

The length $L$ of wedge III is:

$$L = \frac{C}{\tan \alpha_3} \tag{1}$$

According to Terzaghi loose earth pressure theory, the surface will form a loose zone with the width of $2R_1$, and the upper base radius $R_1$ of circular table I is:

$$R_1 = \frac{D}{2} \cot\left(\frac{\pi}{8} + \frac{\varphi}{4}\right) \tag{2}$$

$\varphi$ is the weighting internal friction angle of strata, which is obtained by Eq. (3).

$$\varphi = \frac{\varphi_1 H_1 + \varphi_2 H_2}{H_1 + H_2} \tag{3}$$

Since this paper focuses on effective earth pressure, the total earth pressure brought on by soil weight is the excavation face's limit effective support pressure and the seepage force (Liu et al. 2016) obtained through numerical simulation that the seepage direction in the upper soil is basically vertical, while the seepage direction in the lower wedge is horizontal. So only vertical seepage force is considered when calculating the upper loose earth pressure, and only horizontal seepage force is considered when calculating the limit effective support pressure. Under different burial depths, it can be seen from Figs. 22–24 that the water pressure distribution in the strata is basically same. In the numerical simulations, the seepage gradient along tunnel symmetry plane is the largest. The function of vertical and horizontal water pressure on a symmetric plane is applied to approximate the seepage field distribution in order to guarantee the safe limit effective support pressure. Fig. 37 displays the relationship curve between normalized vertical water pressure and tunnel location.

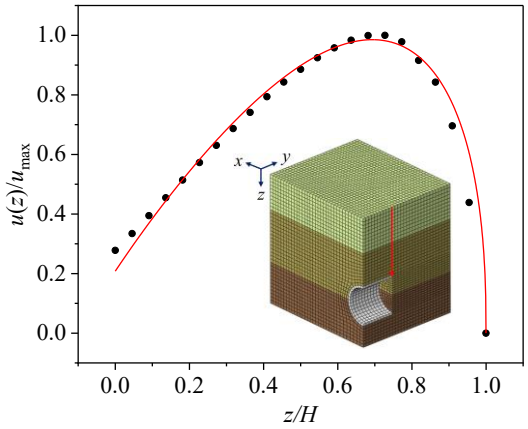


**Fig. 37.** Normalized $u(z)/u_{max}$ and $z/H$ relationship curve.

Here, $z$ is the depth of the strata, $u(z)$ is the water pressure at the depth from the surface, and $u_{max}$ is the maximum of water pressure.

Through dimensional analysis and fitting method, $u(z)$ can be obtained by Eq. (4).

$$u(z) = \gamma_w E \left(\frac{z - H + E}{E}\right)^{0.92} \left(\frac{H}{D}\right)^{0.44} \sin\left(\frac{1 - z}{E}\right)^{0.43} \tag{4}$$

The fit degree in the equation is $R^2 = 0.998$.

The relationship curve between the normalized water head value and the distance

from the excavated face is displayed in Fig. 38 on the central axis in front of the excavated face.

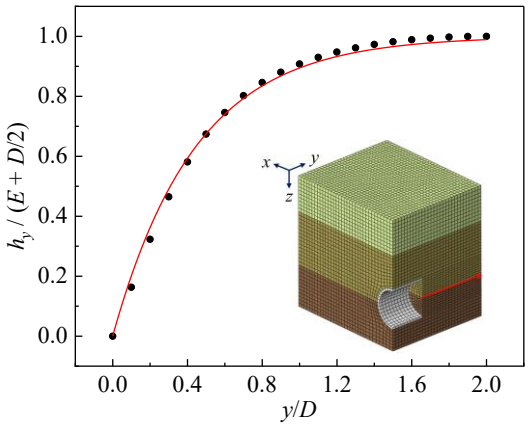


**Fig. 38.** Normalized $h_y$/($E$+$D$/2) and $y$/$D$ relationship curve.

Here, $h_y$ is the water head value at position y in wedge Ⅲ, and $y$ is the distance between a specific position ahead of the tunnel and the excavated face.

Through dimensional analysis and fitting method, $h_y$ can be obtained by Eq. (5).

$$h_y = \left(E + \frac{D}{2}\right)\left(1 - e^{\frac{-0.68y}{D}}\right) \tag{5}$$

The fit degree in the equation is $R^2 = 0.996$.

## 5.2 Analytical formula of the limit effective support pressure

The calculation model of circular table I is shown in Fig. 39.

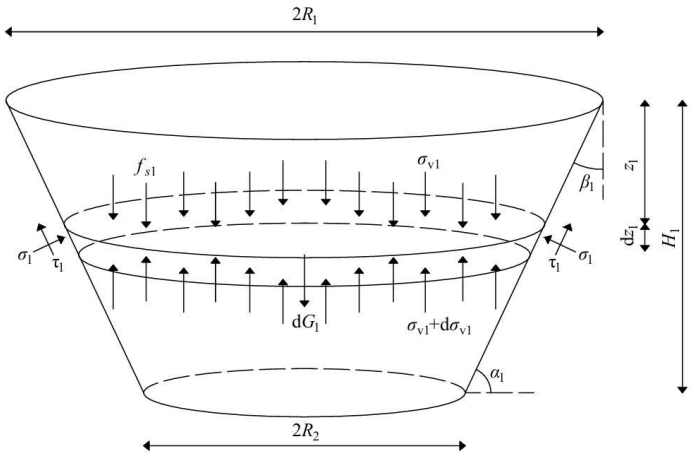


**Fig. 39.** Circular table I calculation model.

In the circular table I, the bottom base radius $R_2$ is:

$$R_2 = R_1 - \frac{H_1}{\tan\alpha_1} \tag{6}$$

The angle $\beta_1$ between the side and the vertical direction is:

$$\beta_1 = 90^\circ - \alpha_1 \tag{7}$$

The thickness of micro-body is d$z_1$, and the distance $z_1$ from the upper surface of micro-body to the surface is:

$$z_1 = z - H_w \tag{8}$$

The area $S_1$ of the upper surface of micro-body is:

$$S_1 = \pi\left(R_1 - z_1 \tan\beta_1\right)^2 \tag{9}$$

The circumference $C_1$ of the upper surface of micro-body is:

$$C_1 = 2\pi\left(R_1 - z_1 \tan\beta_1\right) \tag{10}$$

The saturated unit weight of the slightly-density sandy pebble strata is $\gamma_1$, and the gravity d$G_1$ of micro-body is:

$$\mathrm{d}G_1 = \gamma_1\pi\left(R_1 - z_1 \tan\beta_1\right)^2 \mathrm{d}z_1 \tag{11}$$

The effective lateral pressure coefficient $k_1$ is:

$$k_1 = 1 - \sin\varphi_1 \tag{12}$$

The relation coefficient $K_1$ between normal stress on the side and vertical stress is:

$$K_1 = k_1 \sin^2\alpha_1 + \cos^2\alpha_1 \tag{13}$$

The vertical effective compressive stress is $\sigma_{v1}$, and the uniform distributed seepage force at height $z_1$ is $f_{s1}$. The normal stress $\sigma_1$ on the side is:

$$\sigma_1 = K_1\sigma_{v1} \tag{14}$$

The tangential stress $\tau_1$ on the side is:

$$\tau_1 = K_1\sigma_{v1}\tan\varphi_1 \tag{15}$$

The force balance equation of the micro-body in the vertical direction is as follows:

$$\sigma_{v1}S_1 + \mathrm{d}G_1 = \left(\sigma_{v1} + \mathrm{d}\sigma_{v1}\right)S_1 + \tau_1 C_1 \cos\beta_1 \mathrm{d}z_1 + \sigma_1 C_1 \sin\beta_1 \mathrm{d}z_1 + f_{s1}S_1 \tag{16}$$

When $z_1 = 0$, $\sigma_{v1} = 0$. The Eq. (17) is obtained by bringing this boundary condition into the Eq. (16).

413
$$\sigma_{v1}=\frac{\gamma_1\left(R_1-z_1\tan\beta_1\right)}{A_1}\left(1-\mathrm{e}^{\frac{-A_1z_1}{R_1-z_1\tan\beta_1}}\right)+2\left(E-H\right)\gamma_w\mathrm{e}^{\frac{-A_1z_1}{R_1-z_1\tan\beta_1}}+\frac{A_1}{R_1-z_1\tan\beta_1}\int_0^{H_1}u\left(z\right)\mathrm{e}^{\frac{A_1z_1}{R_1-z_1\tan\beta_1}}\mathrm{d}z_1\mathrm{e}^{\frac{-A_1z_1}{R_1-z_1\tan\beta_1}} \tag{17}$$

414 Here, $A_1=2K_1\left(\tan\varphi_1\cos\beta_1+\sin\beta_1\right)$. In Eq. (17), the former one is the loose earth

415 pressure without considering the seepage, and the latter two are the increase terms

416 caused by the seepage force.

417 Then the vertical stress $q_1$ of circular table I acting on circular table II is:

418
$$q_1=\frac{\gamma_1R_2}{A_1}\left(1-\mathrm{e}^{\frac{-A_1H_1}{R_2}}\right)+2\gamma_wH_w\mathrm{e}^{\frac{-A_1H_1}{R_2}}+\frac{A_1}{R_2}\int_0^{H_1}u\left(z\right)\mathrm{e}^{\frac{A_1z_1}{R_1-z_1\tan\beta_1}}\mathrm{d}z_1\mathrm{e}^{\frac{-A_1H_1}{R_2}} \tag{18}$$

419 The calculation model of circular table II is shown in Fig. 40.

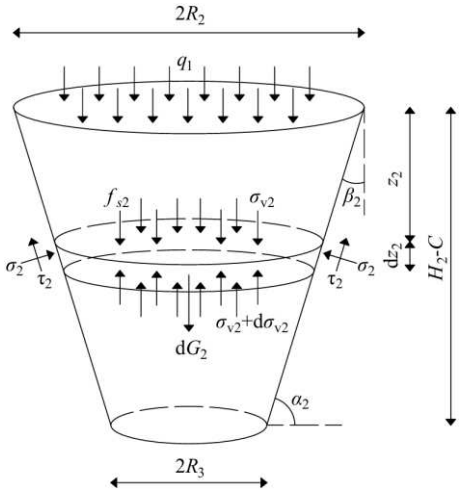


**Fig. 40.** Circular table II calculation model.

420 Based on the area equivalency principle, the bottom base radius $R_3$ in the circular table

421 Ⅱ is:

422
$$R_3=\sqrt{\frac{BL}{\pi}} \tag{19}$$

423 The inclination angle $\alpha_2$ of circular table is:

424
$$\alpha_2=\arctan\frac{H_2-C}{R_2-R_3} \tag{20}$$

425 The angle $\beta_2$ between the side and the vertical direction is:

426
$$\beta_2=90^\circ-\alpha_2 \tag{21}$$

The thickness of micro-body is d$z_2$, and the distance $z_2$ from the upper surface of micro-body to the surface is:

$$z_2 = z - H_w - H_1 \tag{22}$$

The effective lateral pressure coefficient $k_2$ is:

$$k_2 = 1 - \sin\varphi_2 \tag{23}$$

The relation coefficient $K_2$ between normal stress on the side and vertical stress is:

$$K_2 = k_2 \sin^2\alpha_2 + \cos^2\alpha_2 \tag{24}$$

Similarly, according to the analysis steps of circular table I, the force analysis of the micro-body in circular table II is carried out.

The vertical stress $q_2$ of circular table II acting on wedge III is:

$$q_2 = \frac{\gamma_2 R_3}{A_2}\left[1 - \mathrm{e}^{\frac{-A_2(H_2-C)}{R_3}}\right] + q_1 \mathrm{e}^{\frac{-A_2(H_2-C)}{R_3}} + \frac{A_2}{R_3}\int_0^{H_2-C} u(z)\,\mathrm{e}^{\frac{A_2 z_2}{R_2 - z_2\tan\beta_2}}\mathrm{d}z_2\,\mathrm{e}^{\frac{-A_2(H_2-C)}{R_3}} \tag{25}$$

Here, $A_2 = 2K_2\left(\tan\varphi_2\cos\beta_2 + \sin\beta_2\right)$.

The calculation model of wedge III is shown in Fig. 41.

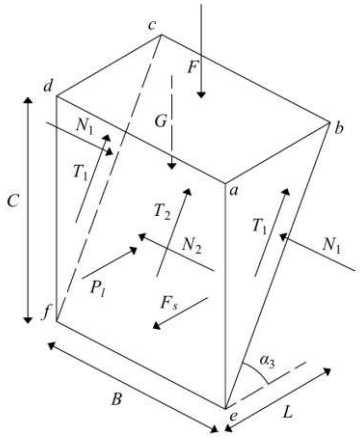


**Fig. 41.** Wedge III calculation model.

In Fig. 41, the force $F$ of circular table II acting on wedge III is:

$$F = q_2 S_3 \tag{26}$$

Here, the bottom area of circular table II is $S_3$, and $S_3 = \pi R_3^2$.

The hydraulic gradient is obtained by Eq. (5) and integrated in wedge III. The horizontal seepage force $F_s$ is:

$$F_s = -\gamma_w \left[ 0.39L + \frac{0.68EL}{D} \right] \times \int_0^{\frac{L}{\tan\alpha_3}} \left( L - y\tan\alpha_3 \right) e^{\frac{-0.68y}{D}} dy \tag{27}$$

The wedge Ⅲ's gravity G is:

$$G = \frac{1}{2} BCL\gamma_2 \tag{28}$$

Here, $\gamma_2$ is the saturated unit weight of the medium dense sandy pebble stratum.

The friction force $T_1$ acting on the side of wedge III is:

$$T_1 = S_c \tau_c \tag{29}$$

Here, the side area of wedge III is $S_c$, $S_c = \frac{1}{2} CL$ .The tangential stress acting on the side of wedge is $\tau_c$, $\tau_c = k_2 \left( q_2 + \frac{\gamma_2 C}{3} \right) \tan\varphi_2$, and $k_2 = 1 - \sin\varphi_2$.

On the side of wedge Ⅲ, the pressure $N_1$ is:

$$N_1 = \frac{T_1}{\tan\varphi_2} \tag{30}$$

The relationship between the friction force $T_2$ and the pressure $N_2$ acting on the sliding surface of wedge III can be obtained by Eq. (31).

$$T_2 = N_2 \tan\varphi_2 \tag{31}$$

The force analysis of wedge III is carried out, and the equation for force balance in the horizontal direction is as follows:

$$P_l + 2T_1 \cos\alpha_3 + T_2 \cos\alpha_3 = N_2 \sin\alpha_3 + F_s \tag{32}$$

In Eq. (32), $P_l$ is the excavation face's maximum effective support pressure.

The following is the force balance equation in the vertical direction:

$$F + G = 2T_1 \sin\alpha_3 + T_2 \sin\alpha_3 + N_2 \cos\alpha_3 \tag{33}$$

The parameters in Eqs. (26) to (31) are substituted into Eqs. (32) to (33), and the limit effective support pressure $P_l$ is:

$$P_l = \delta \left( F + G - 2T_1 \sin\alpha_3 \right) + F_s - 2T_1 \cos\alpha_3 \tag{34}$$

Here, $\delta = \frac{\sin\alpha_3 \cot\varphi_2 - \cos\alpha_3}{\sin\alpha_3 + \cos\alpha_3 \cot\varphi_2}$.

**5.3 Verification of theoretical calculation results**

For the lower dense and upper loose saturated sandy pebble stratum, the excavated face deformation occurs in medium dense sandy pebble stratum. The relationship between the upper loose soil and support force should be the primary focus when evaluating the stability of the excavation face.

According to the theoretical computation, the excavation face's limit effective support compressive stress $\sigma_l$ is:

$$\sigma_l = \frac{P_l}{BC} \tag{35}$$

Here, $B = D$ and $C = \frac{D}{2}$.

The difference between the average water pressure and the average saturated earth pressure on the upper half of the excavation face is represented by $\sigma_l$ in model tests. The average value of earth pressure boxes No. 1, No. 2, No. 3, and No. 6 is used to calculate the saturated earth pressure. The average reading from the No. 1, No. 2, and No. 5 osmometers is used to calculate the water pressure.

Fig. 42 compares the results of model tests with those of theoretical calculations. The limit effective support compressive stress determined by theoretical calculation progressively rises to 1.882 kPa, 2.227 kPa, and 2.431 kPa, respectively, as the buried depth increases. The limit effective support compressive stress obtained by model test also gradually increases to 2.007 kPa, 2.332 kPa and 2.747 kPa, respectively. The findings indicate that as buried depth increases, so does the limit effective support compressive stress. Under the same burial depth condition, model test results are greater than theoretical calculation results. This is because the baffle is subjected to the friction resistance of the circular aluminum cylinder in the test process, resulting in a larger support force on the excavated face. The accuracy of the theoretical calculation model is confirmed by the good agreement between the theoretical calculation results and the model test results, with an error of less than 12%.

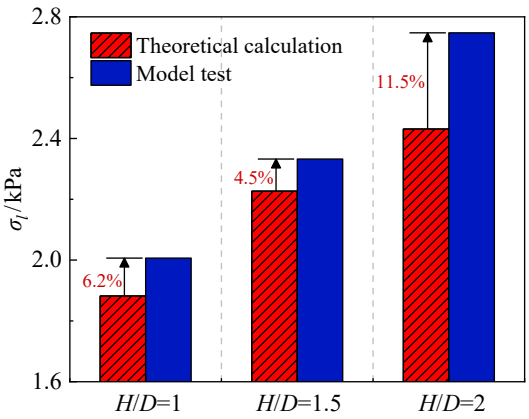


**Fig. 42.** Comparison of the results of model test and theoretical calculation.

## 6 Conclusions

The stability of the excavation face under different buried depths is examined in this paper using numerical simulations and model tests for the upper loose saturated sandy pebble strata and lower dense strata. Based on DIC technology, the excavated face's progressive failure process with active instability is analyzed, and the theoretical calculation model of excavation face is presented. In the meantime, the analytical formula of the limit effective support force of the excavated face taking seepage impact into account is derived, and the fitted seepage force formula is introduced into theoretical calculation. The main conclusions are as follows.

(1) The change process of peak displacement is separated into three stages based on the change law of highest displacement of ground settlement with $L$ under various buried depth conditions. There are no settlement stage, slow settlement stage and rapid settlement stage respectively. With the decrease of the buried depth, there is a gradual increase in both the magnitude and extent of ground settlement.

(2) The water pressure in front of the excavation face shows a trend of first rising and then stabilizing with the increase of $L$ under various burial depth conditions. The decrease of buried depth will increase the seepage velocity of water in the strata, while having no effect on the seepage path range of water.

(3) Accordingly, the equivalent L in the limit equilibrium condition is 3.5 cm, 2.5 cm, and 1.9 cm as the buried depth decreases. This result implies that the general instability of the stratum will occur beforehand as the buried depth decreases.

(4) With the decrease of buried depth, the range and degree of strata instability increase gradually. When the overall instability of the stratum happens, an excavation face instability model of "quarter ellipsoid + double circular table" is formed. Compared

with the homogeneous sandy pebble strata, the instability area of lower dense and upper loose stratum is larger.

(5) The theoretical calculation model of excavation face is composed of circular table I, circular table II and wedge III. The excavation face's limit effective support compressive stress rises as the buried depth does.

## Data Availability

Data supporting this research article are available from the corresponding author on request.

## Declaration of Competing Interest

The authors declare that they have no known competing financial interests or personal relationships that could have appeared to influence the work reported in this paper.


## Acknowledgements

The authors would like to respect and thank all reviewers for their constructive and helpful review.

## Funding

The authors gratefully acknowledge the financial support provided by the National Natural Science Foundation of China (No. 52278382) and Natural Science Foundation of Beijing Municipality (No. 8222004).


## References


Alagha ASN, Chapman DN (2019) Numerical modelling of tunnel face stability in homogeneous and layered soft ground. Tunnelling and Underground Space Technology 94:103096. https://doi.org/10.1016/j.tust.2019.103096

Antão AN, Vicente Da Silva M, Monteiro N, Deusdado N (2021) Upper and lower bounds for three-dimensional undrained stability of shallow tunnels. Transportation Geotechnics 27:100491. https://doi.org/10.1016/j.trgeo.2020.100491

Mi B, Xiang Y (2020) Model experiment and calculation analysis of excavation-seepage stability for shallow shield tunneling in sandy ground

Chen R, Yin X, Tang L, Chen Y (2018) Centrifugal model tests on face failure of earth pressure balance shield induced by steady state seepage in saturated sandy silt ground. Tunnelling and Underground Space Technology 81:315–325. https://doi.org/10.1016/j.tust.2018.06.031

Chen X, Hu Y, Yao K, Leal Sousa R (2024) Large-deformation finite-element modelling of face instability during tunnelling in clayey soils: Incorporating dynamic excavation process. Tunnelling and Underground Space Technology 153:106038. https://doi.org/10.1016/j.tust.2024.106038

Cheng C, Jia P, Ni P, et al (2023a) Upper bound analysis of longitudinally inclined EPB shield tunnel

face stability in dense sand strata. Transportation Geotechnics 41:101031. https://doi.org/10.1016/j.trgeo.2023.101031

Cheng C, Yang H, Jia P, et al (2023b) Face stability of shallowly buried large-section EPB box jacking crossing the Beijing-Hangzhou Grand Canal. Tunnelling and Underground Space Technology 138:105200. https://doi.org/10.1016/j.tust.2023.105200

Cui X, Li P, Chen Y, et al (2025a) Analysis of face stability for a shield tunnel in the inclined strata with soft upper and hard lower layers. Alexandria Engineering Journal 125:677–691. https://doi.org/10.1016/j.aej.2025.04.013

Cui X, Li P, Ge Z, et al (2025b) Experimental study on face stability of shield tunnel in water-rich inclined composite strata considering different inclination angles. Applied Ocean Research 154:104323. https://doi.org/10.1016/j.apor.2024.104323

Cui X, Li P, Wang C, et al (2025c) Effect of seepage flow on face stability for a tunnel in water-rich silty clay overlying sandy cobble strata. Tunnelling and Underground Space Technology 161:106539. https://doi.org/10.1016/j.tust.2025.106539

Cui X, Li P, Wu J, Wei Y (2024) Stability Analysis of a Shield Tunnel in Unsaturated Soil Considering the Soil Arch Effect. Int J Geomech 24:04024041. https://doi.org/10.1061/IJGNAI.GMENG-8709

Di Q, Li P, Zhang M, et al (2022) Analysis of face stability for tunnels under seepage flow in the saturated ground. Ocean Engineering 266:112674. https://doi.org/10.1016/j.oceaneng.2022.112674

Di Q, Li P, Zhang M, et al (2024) Experimental study on the effect of seepage flow on the tunnel face stability in the saturated ground. Ocean Engineering 299:117074. https://doi.org/10.1016/j.oceaneng.2024.117074

Di Q, Li P, Zhang M, Cui X (2023) Experimental investigation of face instability for tunnels in sandy cobble strata. Underground Space 10:199–216. https://doi.org/10.1016/j.undsp.2022.10.004

Ding W, Liu K, Shi P, et al (2019) Face stability analysis of shallow circular tunnels driven by a pressurized shield in purely cohesive soils under undrained conditions. Computers and Geotechnics 107:110–127. https://doi.org/10.1016/j.compgeo.2018.11.025

Ding X, Li K, Xie Y, Liu S (2022) Face stability analysis of large shield-driven tunnel in rock-soil interface composite formations. Underground Space 7:1021–1035. https://doi.org/10.1016/j.undsp.2022.01.007

Fu Y, Zeng D, Xiong H, et al (2022) Seepage effect on failure mechanisms of the underwater tunnel face via CFD–DEM coupling. Computers and Geotechnics 146:104591. https://doi.org/10.1016/j.compgeo.2021.104591

Ge C, Yang M, Li P, et al (2024) Performance and environmental impacts of deep foundation excavation in soft soils: A field and modeling-based case study in Nanjing, China. Underground Space 18:218–238. https://doi.org/10.1016/j.undsp.2024.01.002

Habumuremyi P, Xiang Y (2023) A 3-D analytical continuous upper bound limit analysis for face stability of shallow shield tunneling in undrained clays. Computers and Geotechnics 164:105779. https://doi.org/10.1016/j.compgeo.2023.105779

Han K, Wang L, Su D, et al (2021) An analytical model for face stability of tunnels traversing the

fault fracture zone with high hydraulic pressure. Computers and Geotechnics 140:104467. https://doi.org/10.1016/j.compgeo.2021.104467

Hou CT, Yang XL (2022) 3D stability analysis of tunnel face with influence of unsaturated transient flow. Tunnelling and Underground Space Technology 123:104414. https://doi.org/10.1016/j.tust.2022.104414

Hu X, Fu W, Woody Ju J, et al (2021) Face stability conditions in granular soils during the advancing and stopping of earth-pressure-balanced-shield machine. Tunnelling and Underground Space Technology 109:103755. https://doi.org/10.1016/j.tust.2020.103755

Jia Z, Bai Y, Liu C, et al (2023) Visualization investigation on stability of shield tunnel face with transparent soil, considering different longitudinal inclination angles. Tunnelling and Underground Space Technology 137:105154. https://doi.org/10.1016/j.tust.2023.105154

Kong D, Teng S, Shi J, Zhao M (2024) An Improved Failure Model Considering the Arching Effect for Tunnel Face Stability in a Weak and Fractured Rock Mass. Int J Geomech 24:04024094. https://doi.org/10.1061/IJGNAI.GMENG-9028

Lei H, Xu Y, Liu M, Zhong H (2024) Face Stability Analysis of Shield Tunnel in Cohesive–Frictional Soils Considering Soil Arch Evolution. Int J Geomech 24:04024275. https://doi.org/10.1061/IJGNAI.GMENG-9391

Li P, Cui X, Xia J, Wang X (2023) Analytical solutions of limit support pressure and vertical earth pressure on cutting face for tunnels. Underground Space 12:65–78. https://doi.org/10.1016/j.undsp.2023.02.004

Li P, Wang C, Cui X, et al (2025) Experimental investigation on the stability of shield tunnel excavation face in upper loose and lower dense water-rich strata. J Zhejiang Univ Sci A 26:471–491. https://doi.org/10.1631/jzus.A2400309

Li W, Zhang C, Tan Z, Ma M (2021) Effect of the seepage flow on the face stability of a shield tunnel. Tunnelling and Underground Space Technology 112:103900. https://doi.org/10.1016/j.tust.2021.103900

Lin Q, Lu D, Lei C, et al (2021) Model test study on the stability of cobble strata during shield under-crossing. Tunnelling and Underground Space Technology 110:103807. https://doi.org/10.1016/j.tust.2020.103807

Liu Q, Liu Z, Xue Y, et al (2024) Deformation features and failure mechanism of subsea shield tunnels with different burial depths crossing fault-zone. Marine Georesources & Geotechnology 42:679–693. https://doi.org/10.1080/1064119X.2023.2214132

Liu W, Albers B, Zhao Y, Tang X (2016) Upper bound analysis for estimation of the influence of seepage on tunnel face stability in layered soils. J Zhejiang Univ Sci A 17:886–902. https://doi.org/10.1631/jzus.A1500233

Liu X, Wang F, Fang H, Yuan D (2019) Dual-failure-mechanism model for face stability analysis of shield tunneling in sands. Tunnelling and Underground Space Technology 85:196–208. https://doi.org/10.1016/j.tust.2018.12.003

Lu X, Zhou Y, Huang M, Li F (2017) Computation of the Minimum Limit Support Pressure for the Shield Tunnel Face Stability Under Seepage Condition. Int J Civ Eng 15:849–863. https://doi.org/10.1007/s40999-016-0116-0

Lü X, Zhou Y, Huang M, Zeng S (2018) Experimental study of the face stability of shield tunnel in

sands under seepage condition. Tunnelling and Underground Space Technology 74:195–205. https://doi.org/10.1016/j.tust.2018.01.015

Ma S, Duan Z, Huang Z, et al (2022a) Study on the stability of shield tunnel face in clay and clay-gravel stratum through large-scale physical model tests with transparent soil. Tunnelling and Underground Space Technology 119:104199. https://doi.org/10.1016/j.tust.2021.104199

Ma S, Li J, Li Z (2022b) Critical support pressure of shield tunnel face in soft-hard mixed strata. Transportation Geotechnics 37:100853. https://doi.org/10.1016/j.trgeo.2022.100853

Tu S, Li W, Zhang C, et al (2024) Model test and discrete element method simulation of tunnel face stability in sand-gravel inclined layered stratum. Computers and Geotechnics 172:106456. https://doi.org/10.1016/j.compgeo.2024.106456

Wang C, Hou J, Ye X-W, et al (2023a) A 3D torus-slice model for limit equilibrium analysis of shield tunnel face under soil arching effect. Engineering Failure Analysis 146:107148. https://doi.org/10.1016/j.engfailanal.2023.107148

Wang F, Du X, Li P (2023b) Predictions of ground surface settlement for shield tunnels in sandy cobble stratum based on stochastic medium theory and empirical formulas. Underground Space 11:189–203. https://doi.org/10.1016/j.undsp.2023.01.003

Wang J, Lin G, Xu G, et al (2022) Face stability of EPB shield tunnels in multilayered ground with soft sand lying on hard rock considering dynamic excavation process: A DEM study. Tunnelling and Underground Space Technology 120:104268. https://doi.org/10.1016/j.tust.2021.104268

Wang J, Tian N, Lin G, et al (2024) Face failure of deep EPB shield tunnels in dry graded cobble-rich soil: A DEM study. Tunnelling and Underground Space Technology 147:105622. https://doi.org/10.1016/j.tust.2024.105622

Wang L, Han K, Xie T, Luo J (2019) Calculation of Limit Support Pressure for EPB Shield Tunnel Face in Water-Rich Sand. Symmetry 11:1102. https://doi.org/10.3390/sym11091102

Weng X, Sun Y, Yan B, et al (2020) Centrifuge testing and numerical modeling of tunnel face stability considering longitudinal slope angle and steady state seepage in soft clay. Tunnelling and Underground Space Technology 101:103406. https://doi.org/10.1016/j.tust.2020.103406

Wong KS, Ng CWW, Chen YM, Bian XC (2012) Centrifuge and numerical investigation of passive failure of tunnel face in sand. Tunnelling and Underground Space Technology 28:297–303. https://doi.org/10.1016/j.tust.2011.12.004

Yang F, Qin A, Zheng X, et al (2024) Stability and Failure Mechanism of the Tunnel Face in Nonhomogeneous Clay with Longitudinal Slopes: A Kinematic Limit Analysis. Int J Geomech 24:04024212. https://doi.org/10.1061/IJGNAI.GMENG-9782

Yang X-L, Zhong J-H (2019) Stability Analysis of Tunnel Face in Nonlinear Soil under Seepage Flow. KSCE Journal of Civil Engineering 23:4553–4563. https://doi.org/10.1007/s12205-019-0601-5

Ye Z, Wu H, Wang C, et al (2022) Limit face pressure analysis of an EPB shield under suffusion conditions. Tunnelling and Underground Space Technology 130:104733. https://doi.org/10.1016/j.tust.2022.104733

Yi C, Senent S, Jimenez R (2019) Effect of advance drainage on tunnel face stability using Limit Analysis and numerical simulations. Tunnelling and Underground Space Technology

93:103105. https://doi.org/10.1016/j.tust.2019.103105
Yin X, Chen R, Meng F (2021) Influence of seepage and tunnel face opening on face support pressure of EPB shield. Computers and Geotechnics 135:104198. https://doi.org/10.1016/j.compgeo.2021.104198
Zhang D, Ma Z, Yu B, Yin H (2019) Upper bound solution of surrounding rock pressure of shallow tunnel under nonlinear failure criterion. J Cent South Univ 26:1696–1705. https://doi.org/10.1007/s11771-019-4126-3
Zhang S, Cheng X, Qi L, Zhou X (2022a) Face stability analysis of large diameter shield tunnel in soft clay considering high water pressure seepage. Ocean Engineering 253:111283. https://doi.org/10.1016/j.oceaneng.2022.111283
Zhang Y, Tao L, Zhao X, et al (2022b) An analytical model for face stability of shield tunnel in dry cohesionless soils with different buried depth. Computers and Geotechnics 142:104565. https://doi.org/10.1016/j.compgeo.2021.104565
Zhao Y, Yang Z, Chen Z, Ling D (2024) A Modified Wedge-Prism Model for Calculating the Limit Support Pressure of a Shallow Shield Tunnel Face in Unsaturated Sandy Soil. Int J Geomech 24:04024233. https://doi.org/10.1061/IJGNAI.GMENG-10131